Thesis for the degree of Doctor of Philosophy

Direct conversion of methane to methanol: transition-metal dimer sites in small-pore zeolites

First-principles calculations and microkinetic modeling

UNNI ENGEDAHL

CHALMERS

Department of Physics

Chalmers University of Technology

Gothenburg, Sweden 2021

Direct conversion of methane to methanol:
transition-metal dimer sites in small-pore zeolites
First-principles calculations and microkinetic modeling
UNNI ENGEDAHL
ISBN 978-91-7905-565-3

Doktorsavhandlingar vid Chalmers tekniska högskola
Ny serie nr. 5032
ISSN 0346-718X

Department of Physics
Chalmers University of Technology
SE-412 96 Gothenburg
Sweden
Telephone: +46 (0)31-772 1000

Cover:
Depending on what you see, either the tetrahedral building block of the zeolite, or a molecule with five atoms, e .g. methane.

Printed at Chalmers Digitaltryck
Gothenburg, Sweden 2021

Direct conversion of methane to methanol:
transition-metal dimer sites in small-pore zeolites
First-principles calculations and microkinetic modeling

UNNI ENGEDAHL
Department of Physics
Chalmers University of Technology

Abstract

Direct conversion of methane to methanol is a highly desired reaction. Partially oxidizing methane into a liquid fuel at ambient temperature and pressure would enable utilization of natural gas and biogas to a much larger extent than what is possible today. This is desirable since natural gas is the cleanest fossil energy source, and when in the form of biogas (or biomethane) has a net-zero carbon emission. The direct conversion of methane requires a catalyst; however, no material with high enough activity and selectivity towards methanol has been identified. Mimicking the enzyme methane monooxygenase (MMO), copper-exchanged zeolites are considered promising candidates. A plethora of different active sites have been suggested, but neither the detailed structure and composition of the active site, nor the mechanism for the reaction, are known. In this thesis, the catalytic properties of transition metal dimers in small-pore zeolites are studied using first-principles calculations, ab initio thermodynamics, and microkinetic modeling. As a first step, the stability of the Cu dimer structure in SSZ-13 is investigated under direct conversion conditions. The zeolite is found to be very humid, and the structure of the proposed active site is highly dependent on the temperature and partial pressure of relevant gases. The Cu_2O and Cu_2OH structures are found to be the energetically most preferred. The reaction over the sites is limited by a high free energy barrier of the C-H bond in methane and a slow methanol desorption rate. Adding water to the reaction facilitates desorption of the products, increasing the activity of the Cu_2O site. The reaction mechanism for an entire reaction cycle over the Cu-dimer, including the formation of the active site, is investigated in dry and wet conditions. The oxidation of the Cu monomers, using molecular oxygen, is limited by the diffusion of the Cu species along the zeolite framework and the activity is increased when water is added to the reaction. To further investigate the composition of the active dimer site, transition-metal and transition-metal alloy configurations are investigated. The adsorption energy of atomic oxygen is identified as a descriptor for the activity of the dimer systems. Identified motifs showing activity towards direct methane-to-methanol conversion are the 2Cu, along with the AuPd and PdCu alloy dimer systems. The activity of these systems is comparable and, when excluding competing reactions, meets the high turn-over needed for a commercially viable catalyst.

Keywords: partial methane oxidation, density functional theory, microkinetic modeling, zeolites, CHA, SSZ-13, transition metals, alloy

List of Publications

This thesis is based on the following appended papers:

Paper I

First-Principles Study of Oxidation State and Coordination of Cu-Dimers in Cu-SSZ-13 During Methane-to-Methanol Reaction Conditions

U. Engedahl, H. Grönbeck, and A. Hellman

Journal of Physical Chemistry C. 2019 Vol. 123 (43), p. 26145-26150

Paper II

Reaction Mechanism for Methane-to-Methanol in Cu-SSZ-13: First-Principles Study of the $Z_2[Cu_2O]$ and $Z_2[Cu_2OH]$ Motifs in the Small-Pore Zeolite Chabazite

U. Engedahl, A. A. Arvidsson, H. Grönbeck, and A. Hellman

Catalysts 2021 Vol. 11, p. 17

Paper III

Complete Reaction Cycle for Methane-to-Methanol Conversion over Cu-SSZ-13: First-Principles Calculations and Microkinetic Modeling

U. Engedahl, A. Boje, H. Ström, H. Grönbeck, and A. Hellman

Journal of Physical Chemistry C. 2021 Vol. 125, p. 14681-14688

Paper IV

Transition Metal Alloys: Investigating the Composition of the Dimer Site in Chabazite for Direct Methane-to-Methanol Conversione

U. Engedahl, A. Boje, H. Ström, H. Grönbeck, and A. Hellman

In manuscript

My contributions to the publications

Paper I
I performed all calculations and wrote the first draft of the manuscript. I was responsible for the writing process, the manuscript submission and answering the reviewers' comments on the manuscript.

Paper II
I performed all DFT calculations and wrote the first draft of the manuscript. I was responsible for the writing process, the manuscript submission and answering the reviewers' comments on the manuscript.

Paper III
I performed all DFT calculations and co-wrote the first draft of the manuscript. I was responsible for the writing process, the manuscript submission and answering the reviewers' comments on the manuscript.

Paper IV
I performed all DFT calculations and co-wrote the first draft of the manuscript.

Contents

Chapter 1

Introduction

As the human population increases and the standard of living is being raised worldwide, the projected future energy demand is significantly higher than today. Available clean energy is a prerequisite for combating challenges like poverty, food and water shortages, and the effects of environmental changes. However, meeting this increased demand for a population of 8, or eventually maybe 10 billion people, will require a viable revolution in the way energy is produced. As of now, the world is reliant on energy from fossil sources, sources that will eventually run out or be of such poor quality that they will no longer reliably supply the needed quantity. This reliance on non-renewable energy sources is not only a matter of depletion of resources but also of changing our living conditions, as carbon-deposits are being released into the atmosphere. As greenhouse-gases, e.g. methane, carbon-dioxide, and water vapor, act to trap heat in the atmosphere. An increase in the concentration of these gases leads to an increase in the global temperature, which will, in turn, affect the habitat of all life on the planet. A shift away from these traditional non-renewable energy sources has already commenced. However, the world is shaped around the dependency on oil, and regardless of whether the end goal is a society only relying on renewable resources, or if a combination of energy sources (both perishable and non-perishable) is appropriate, wasteful energy management should be minimized. Thus, as a step towards a more sustainable, high output energy sector, the efficiency of currently available energy sources should be improved.

The matter of energy production and consumption is not only a question of emission and pollution. It is also a matter of fully utilizing the available fuel reserves. Technological advances built to match the already existing infrastructure and end-usage encourage an immediate increase in environmentally more sustainable energy production, and the utilization of discarded byproducts leads to an increased production simply due to a reduction in waste. Therefore, identifying areas where improvements are imperative and finding solutions with a straightforward application is where the advances must occur.

Using Global Warming Potentials (GWP) [1] as a measurement of how much a gas impacts the increasing global temperature, CO_2 is the reference, given an impact of 1. This impact is a combination of the gas' energy storing ability and the average amount of time the gas remains in the atmosphere after being released. As a greenhousegas, methane has a GWP of 28-36 over a 100-year period. Meaning it has an impact on the global warming approximately 30 times more severe than CO_2. Thus, to quickly limit or reverse the change in climate brought on by the burning of fossil fuel, better management and utilization of methane should be prioritized. According to the International Energy Agency (IEA), reducing methane emissions from the oil and gas industry is the most cost-effective and impactful action available to achieve global climate goals [2].

One way to not only reduce the amount of methane released into the atmosphere, but also utilizing its energy content is by turning the gas into an easily manageable and usable liquid fuel. If a method for direct conversion of methane into methanol is developed, the methane, which is today vented or flared at oil extraction sites, would be utilized in the current energy system. However, the direct partial oxidation of methane is a challenging reaction, with no known efficient catalyst. In the development of new catalytic candidates for the reaction, attention has been given to the mineral-like silica/alumina-based solids called zeolite. The porous structure of the zeolites and the acidity of its cages are used in both oil refinery (fluid catalytic cracking) and NO_x treatment (selective catalytic reduction). The zeolites exist in a wide variety of structures and detailed composition, enabling finely tuned catalytic properties.

Chapter 2

Catalysis

This is not the first time the emergence of a more modern society has placed demands for fundamental changes to the way we produce energy. Ever since the human population left the hunter/gatherer life and settled down to farm the land, the availability of free, fertile land for growing crops set the limit to how large the human population could grow. When there was no more land to harvest, no more people could be fed. This all changed at the beginning of the 20th century.

Crops need nitrogen to grow, it takes this from the ground and when harvest comes, the nitrogen in the plants is removed. Since most plants cannot take nitrogen from the air, the limited amount of nitrogen in the soil dictated how much crops could be grown. This was the case until 1908, when Fritz Haber and Carl Bosch were able to convert gaseous nitrogen and hydrogen into ammonia using metal catalysts under high pressure and temperature [3]. This is the basis for modern-day fertilizer, which replenish the nitrogen in the soil, and more nitrogen in the ground means more crops. The catalytic reaction

$$\mathrm{N_2} + 3\mathrm{H_2} \longrightarrow 2\,\mathrm{NH_3} \qquad \Delta H = -0.96 \text{ eV}$$

enabled the continued growth of the human population. The same revolutionizing development necessary to meet the growing demand for food in the 19th century is now necessary to meet the rapidly growing demand for energy in the 21st century.

2.1 Catalysts

A catalyst has two fundamental objectives: increasing the activity and the selectivity of a specific reaction. This means that the presence of a catalyst should increase the rate at which a reaction occurs while simultaneously preventing other reactions from occurring. This should be done without consuming or irreversibly changing the catalyst. The site on which the reaction takes place is called an active site [4]. This can be a small cluster or an atom (called single-site catalysts) that has a different structure and composition as compared to the surrounding material. For a heterogeneous catalyst (i.e., a catalyst existing in a different phase than the reactants, e.g., a solid surface promoting a gaseous reaction), the active site acts to gather the reactants together and provide new reaction paths. Controlling the structure and composition of the active site influences the catalytic properties of the material. The catalyst works by creating bonds with the reactants, simultaneously breaking existing intramolecular bonds and providing a lower energy path for the reaction to take place, as illustrated in fig. 2.1. For this approach to have the

desired effect, the bonds created between the catalyst and the reactants can neither be too strong nor too weak, one observation often referred to as the Sabatier's principle [5], [6]. If the bonds between the catalyst and the reactants are too weak, the coverage of the reactants on the catalyst will be too low and the barrier for a reaction too high, resulting in a low conversion. If the bond between the catalyst and any of the intermediate steps in the reaction is too strong, the reaction will not be able to proceed, and the catalyst will become blocked or poisoned.

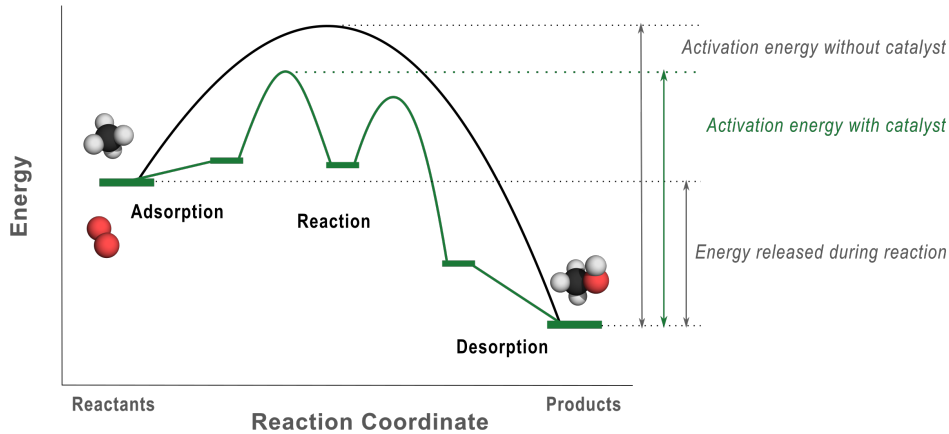

Figure 2.1: The purpose of catalysis is to increase the rate of a desired reaction. By diverting the reaction into a path that divides the process into several steps, the new energy barriers for the reaction are lower than that of the uncatalyzed reaction. There is always a possibility that the catalyst introduces undesired pathways, thereby affecting the selectivity.

One important aspect of the catalytic properties is the interplay between activity and selectivity. The effects of a catalyst only apply to the kinetics of a reaction; it does not affect the thermodynamics. If there are more thermodynamically favored reactions competing with the desirable one, this will not be changed by adding a catalyst. This means that increasing the activity of a reaction can come at the cost of a less favorable selectivity among the products. Among the most selective catalysts are enzymes, able to produce almost exclusively the desired product. This type of naturally occurring (often protein-based) catalyst is called a biocatalyst. In a biocatalyst, there is a geometric component that influences the selectivity; like a puzzle where only the correct piece fits, only one reaction is promoted. Although these catalysts are selective, the activity is generally low. On, for instance, an extended surface catalyst, where this geometric featured is missing or less pronounced, this same effect might be difficult to achieve. However, it might be introduced by adsorbate coverages or alloying. A catalytic material with a porous structure might have additional effects arising from the confinement. For

instance, the selectivity might then be controlled by the catalyst's ability to act as a sieve, in addition to the properties given by the active sites.

2.1.1 Zeolites

Zeolites are a type of microporous crystalline aluminosilicates found both in nature and as manufactured structures. The basic components, or primary building units, are SiO_4 and AlO_4 tetrahedra (or T-sites), working like Lego-pieces to form a wide variety of different framework structures through interlocking O-corner atoms. The primary building blocks are connected to form secondary building units, out of which some examples are seen in fig. 2.2. These are, in turn, repeated and connected into larger structures of cages and channels. The pore sizes, ranging from 4 to 12 membered rings (MRs), are one way to control the accessibility in the material. The well-defined structure of the framework provides a material with a known detailed structure, and thus clearly defined catalytically active site structures. This gives them a close resemblance with enzymes. When constructed of exclusively SiO_4 T-sites, the zeolite framework is chemically inert.

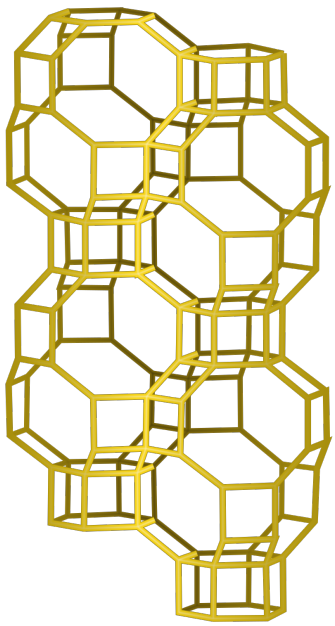

Chabazite (CHA), SSZ-13

4, 6, and 8 MRs

One small and one large cage

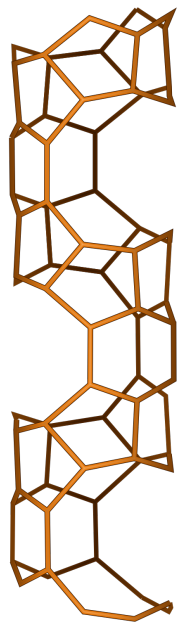

MFI, ZSM-5

4, 5, 6, and 10 MRs

Odd MRs give the structure channels

Figure 2.2: CHA and MFI, two zeolite structures displaying different characteristics [7].

By replacing a Si^{4+} for an ion of either lower or higher charge, the framework becomes prone to catalytic reactions, and the acidity of the structure is changed. When the Si^{4+} is replaced by an Al^{3+}, a charge deficit is introduced into the material. This deficit must be compensated by the insertion of cations, such as H^+, Na^+, or Cu^+. The concentration and relative position of the framework Al^{3+} along with the choice of cation contribute to the characteristics of the zeolite catalyst [8], this all in addition to the effects of which combination of MRs the framework is based on. All these factors play a role in the functionality of the material, and thus its property as a potential catalytic material.

2.1.2 Catalyst Design

The traditional method for developing a new catalyst is empirical, to systematically try different materials until something that enhances the reaction is identified. The same is true when it comes to improving on already existing implemented catalytic systems. This is an approach that has resulted in highly functioning catalysts. In an experimental setting however, the empirical method is very time and resource consuming, as well as extremely complicated. Choosing what to investigate require immense knowledge, both of the reaction to be catalyzed, and of the unique characteristics of the specific active (and non-active) materials. A purely experimental method provides limited information as to why and how the material is promoting the reaction and, thus, limited information as to how the process could be improved. The catalytic properties of a material are, in principle, completely determined by the electronic structure of the material; and ultimately, the goal is to have enough knowledge of what determines the catalytic activity of a material to be able to tailor make what is needed for each reaction, atom-by-atom. The availability of computational methods for investigating structural properties of materials is enabling a much more efficient design process. The computational methods available (such as Density Functional Theory (DFT)) provide detailed information on atomic structure and properties on a variety and quantity of elements unfeasible for experimental investigation. The information gained from the computational investigation would thus provide important guidance for the experimental explorations.

Computational methods use model systems, either clusters composed of a finite number of atoms or ideal infinite surfaces within periodic boundary conditions. The cluster model excludes or limits the effect of support material and long range interactions, while the periodic model is based on repeated elementary (or unit) cells over two or three dimensions to simulate an infinite crystal. For a surface model, each feature on the surface, well defined facets but also edges, corners, steps, and kinks, are treated as independent of each other. Each of the structures contribute to the activity of the material, and the most active will generally dominate [9]. The interaction between the reactants and the surface is fundamental to the kinetics of a system, and the activation energies for elementary surface reactions are strongly correlated with adsorption energies. The electronic structure of the surface determines the variation in adsorption energy between different surfaces and different adsorbates. Thus, the adsorption energy can be changed by inserting, or alloying, another metal into the surface or subsurface layer of the catalyst. To investigate more complex catalytic properties, computational catalysis often utilized descriptors [9]. The use of descriptors is possible due to the existence of property correlation. One example of

this is the correlation between the barrier for CH_4 activation and the hydrogen affinity (E_H), with

$$E_H = E(M_mO_xH_{y+1}) - E(M_mO_xH_y),$$

where $E(M_mO_xH_{y+1})$ and $E(M_mO_xH_y)$ are the formation energies of the reduced and bare active sites respectively. One would thus be able to infer the catalytic activity of a material towards CH_4 activation simply by calculating E_H for the active site [10]. Using a visual representation of the Sabatier's principle, a volcano plot (fig. 2.3), new possible catalytic elements can be inferred through their position along the curve. With, e.g., the descriptor on the x-axis, elements residing close to the top represent good potential candidates.

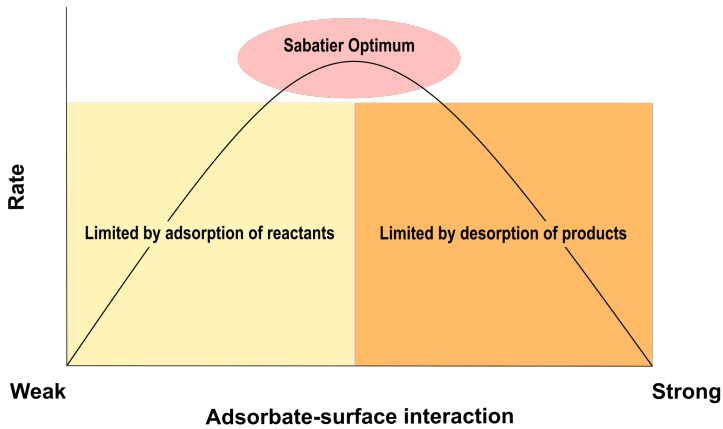

Figure 2.3: A Sabatier volcano plot gives an indication of what elements might be good catalysts for different reaction based on the interaction between the catalyst and the reactants.

Identifying high activity materials is only the first step towards having a new catalyst. Material cost, production cost, long-term stability, resistance to poisons, and lack of side products are equally important factors. These factors are much more difficult, if not impossible, to investigate computationally, and experimental studies are central to the complete development of a technical catalyst. There are limitations to the application of DFT in material research. For one, the method works well for transition metal catalysts, but less so for other classes of materials, such as strongly correlated oxides [11]. In addition, any theoretical model for the calculations will, to some extent, rely on assumptions and simplifications; as in the model system limitations are set to, e.g., the ionic and electronic structure, as well as the configuration of the investigated material. To minimize the human bias in the theoretical design work, e.g., machine learning can be utilized. Supplied with energies and structures provided by DFT, predictions of fictionalized materials not yet known are then made possible.

Chapter 3

Electronic Structure Calculations

The information about the material properties is in the electronic structure. Solving the Schrödinger equation, $\hat{H}\Psi = E\Psi$, of a system will provide its physical and chemical information. For systems of a single electron, this can be done analytically, but all larger systems require a method for gaining the desired electronic structure of the system, while circumventing the need to solve the full Schrödinger equation.

3.1 Density Functional Theory

The complete description of a many-body atomic system is given by the Hamiltonian of the system

$$\hat{H} = \hat{T} + \hat{V}_{ee} + \hat{V}_{eZ} + \hat{V}_{ZZ}, \tag{3.1}$$

where $\hat{T}$ is the kinetic energy operator of the electrons and nuclei, $\hat{V}_{ee}$ is the electron-electron interaction, $\hat{V}_{eZ}$ is the electron-ion interaction, and $\hat{V}_{ZZ}$ is the ion-ion interaction. The first assumption made to simplify the solution to the Schrödinger equation is the Born-Oppenheimer approximation [12]. It assumed that during atomic motion, the electrons instantaneously adapt to the ionic positions without undergoing any transitions between stationary states. The assumption is based on the adiabatic approximation and is rationalized by the much shorter time scale of the electronic motions. The electronic wave function is, thus, decoupled from the nuclei, the electron-nucleic Coulomb interaction is considered as an external potential, and the electronic Hamiltonian becomes

$$\hat{H}_e = \hat{T} + \hat{V}_{ee} + \hat{V}_{eZ}. \tag{3.2}$$

Though decoupled from the nuclei, the electronic Schrödinger equation formed using eq. (3.2) is still computationally expensive. The description possesses one major obstacle, namely the wave function's dependence on the particle positions; the dimensionality of the Schrödinger equation is proportional to the number of electrons in the system.

One way of reducing the complexity of the calculation is by approximating the full wave-function as the product of single particle wave functions, $\Psi(\mathbf{r}_1, \mathbf{r}_2, ..., \mathbf{r}_N) = \psi(\mathbf{r}_1)\psi(\mathbf{r}_2)...\psi(\mathbf{r}_N)$, which is called the Hartree approximation. The energy obtained using this approximation will always be higher than the true ground state energy obtained from the true wave-function. This mean field approximation is not specifically implemented for fermions, and consequently does not satisfy the Pauli-principle. Thus, when calculating the Hartree energy, the electrostatic energy of the electrons, the electron interacting with all electrons in the system, including itself. This causes something called the self-interaction error. The Hartree-Fock method [13]–[15] tries to compensate for this error by approximating

the electronic many-body wave function with a Slater determinant [16] constructed from one-electron wave functions. Thus, enforcing the anti-symmetry of the fermionic system. The interaction that is not included in this spin-interaction (called exchange) is referred to as correlation and is completely neglected. Thus, for systems exhibiting no correlation (such as the single-electron system of H or He^+), Hartree-Fock is an exact method for solving the Schrödinger equation.

Density Functional Theory (DFT) is another way of treating the electronic problem, including an approximation of the exchange and correlation interaction, and with a relatively small computational effort. The theory is based on two theorems formulated by Hohenberg and Kohn [17]:

1. The ground state electronic density, $n_0(\mathbf{r})$, uniquely determines the external potential, $\hat{V}_{ext}$.
2. There exists a functional $E[n(\mathbf{r}), \hat{V}_{ext}]$ for any external potential $\hat{V}_{ext}$ such that the electron density $n(\mathbf{r})$ that minimizes this functional is the exact ground state density.

The ground state energy of a system is, thus, determined by the global minimum value of

$$E[n] = F[n] + \int d\mathbf{r} v_{ext}(\mathbf{r}) n(\mathbf{r}), \tag{3.3}$$

(where v_{ext} is the external potential) subject to the constraint $\int d\mathbf{r} n(\mathbf{r}) = N$, where N is the total number of electrons in the system [18]. By using the electron density, $n(\mathbf{r}) = |\Psi|^2$, a function of three spatial coordinates can replace the myriad of electronic positions in a many-body wave function in eq. (3.2), and the Slater determinant of the Hartree-Fock method. Despite these benefits, the theorems give no explicit expression for the functional, nor a method for how to solve eq. (3.3).

3.1.1 The Kohn-Sham Approach

The difficulty of the introduced functional is the interaction of the particles of the system. The Kohn-Sham ansatz [19] for solving eq. (3.3) replaces the fully interacting many-body system with a system of independent particles. The ansatz has two major benefits: it reduces the complexity by using single particle systems instead of the many-particle original system; and it separates the kinetic energy term and the interaction of the Hartree term in such as way that the non-classical interaction of the electrons, exchange and correlation, is gathered into one term. The Hohenberg-Kohn functional of eq. (3.3) takes the form,

$$E_{KS}[n] = T_0[n(\mathbf{r})] + E_H[n(\mathbf{r})] + \widetilde{E}_{\mathrm{xc}}[n(\mathbf{r})] + \int d\mathbf{r} V_{ext}(\mathbf{r}) n(\mathbf{r}). \tag{3.4}$$

Using this ansatz, the introduced universal functional $F[n(\mathbf{r})]$ on the right hand side in eq. (3.3) contains the contributions of the kinetic energy the non-interacting system (T_0), the classic Coulomb interaction (or Hartree energy, E_H), and the exchange-correlation

energy of the electrons, $\widetilde{E}_{xc}$. Here, the deviation in kinetic energy between the non-interacting system and the original system, along with the unphysical self-interaction error in the Hartree term in eq. (3.4), should here be completely canceled by the exchange-correlation term, $\widetilde{E}_{xc}$. As it stands in eq. (3.4) the Kohn-Sham approach to solving the energy functional is not an approximation. However, the correct exchange-correlation contribution to the functional is unknown.

3.1.2 Exchange-Correlation Approximations

The exchange-correlation term contribution to the total energy is rather small compared to the kinetic and Hartree energy. Still the local, or nearly local, approximations of the functionals of the density required to account for $\widetilde{E}_{xc}$, determine the accuracy of DFT. The exchange-correlation energy can be interpreted as the Coulomb interaction between the electronic density and a positively charged "hole" around the electron caused by the Pauli and Coulomb repulsion [20]. This hole represents a fictitious charge depletion around the electron where the likelihood of finding a second electron is greatly reduced. How to model this charge depletion is a matter of approximations.

Local Density Approximation

In the Local Density Approximation (LDA) [17], [19], the exchange and correlation is assumed to depend only on the local electron density in each point in space, expressed according to

$$E_{\mathrm{xc}}^{\mathrm{LDA}}[n(\mathbf{r})] = \int d\mathbf{r} n(\mathbf{r}) \varepsilon_{\mathrm{xc}}^{\mathrm{LDA}}(n(\mathbf{r})), \tag{3.5}$$

where ε is the energy density per electron at a point $\mathbf{r}$. This can be extended into the Local Spin-Density Approximation (LSDA)[21], [22], taking the electron spin into account. In systems with a slowly varying electron density, such as in the homogeneous electron gas or simple metal-like systems, LDA has proven successful in predicting properties such as bond length. In systems where the electron density varies too rapidly (e.g., molecules) or in strongly correlated systems, the LDA generally overbinds, producing too short bonds and too small lattice parameters [23].

Generalized Gradient Approximation

By including not only the local density but also the change in density, the performance of the exchange-correlation approximation is increased for inhomogeneous materials. A dependence on the electron density gradient is included via an enhancement factor F_{xc}, formulating a semi-local approximation that improves on the LDA called the Generalized Gradient Approximation (GGA) [24], [25]:

$$E_{\mathrm{xc}}^{\mathrm{GGA}}[n(\mathbf{r})] = \int d\mathbf{r} n(\mathbf{r}) \varepsilon_{\mathrm{xc}}^{\mathrm{LDA}}(n(\mathbf{r})) F_{\mathrm{xc}}(n(\mathbf{r}), \nabla n(\mathbf{r})). \tag{3.6}$$

Different GGA functionals have prioritized different behavior of F_{xc} in their description. GGA functionals such as PBE [26] are especially good for atoms and molecules, while PBEsol [27] is adapted to work better for slowly varying densities, i.e., solids.

van der Waals Interaction

The local and semi-local nature of LDA and GGA fail to capture the long-range correlation interaction (called dispersion interaction or van der Waals interaction (vdW) that exists between systems without overlapping charge densities. Between neutral atoms and molecules, the interaction has a behavior of $\sim 1/R^6$ for large R. This long-range effect is especially important in sparse matter. It is possible to account for the vdW forces by empirical parameter fitting [28]–[31]. However, preferably the inclusion of vdW into the functional should be done from first principles. Is the case with vdW-DF, the interaction is calculated in terms of the electron–electron repulsion, resulting in a non-local expression involving the density at two different points:

$$\begin{aligned} E_{\mathrm{xc}}^{\mathrm{vdWDF}} &= E_{\mathrm{x}}^{\mathrm{GGA}} + E_{\mathrm{c}}^{\mathrm{LDA}} + E_{\mathrm{c}}^{\mathrm{nl}}[n], \\ E_{\mathrm{c}}^{\mathrm{nl}}[n] &= \frac{1}{2}\int d\mathbf{r}d\mathbf{r}' n(\mathbf{r})\phi(\mathbf{r},\mathbf{r}')n(\mathbf{r}'), \end{aligned} \tag{3.7}$$

where ϕ is a vdW interaction kernel derived from formal many-body calculation of the electron gas [32]–[34]. This allows for including vdW-interaction self-consistently in DFT.

Hybrid Functionals

The exact exchange energy of Hartree-Fock, E_x^{HF}, can be included into the functional to improve its performance. However, although E_x^{HF} is one-electron self-interaction free, it still does not include any correction for the correlation of self-interaction. Therefore, the Hartree-Fock contribution and the contribution of an approximated DFT functional can be combined:

$$E_{\mathrm{xc}}^{\mathrm{hyb}} = E_{\mathrm{xc}}^{\mathrm{DFT}} + \alpha(E_{\mathrm{x}}^{\mathrm{HF}} - E_{\mathrm{x}}^{\mathrm{DFT}}). \tag{3.8}$$

In this, so-called, hybrid functional [35], E_x^{DFT} is the exchange part of the density functional, calculated with a chosen xc functional. This mixing of exact and approximated exchange energies enables the approximation to improve the calculation of properties for which LDA and GGA are not sufficient. The value of the constant α in eq. (3.8) is often chosen after fitting against experimental data sets [35], [36], resulting in one choice of α being suitable for one particular type of system.

DFT+U - Hubbard Corrections

Another way of compensating for the difficulty of LDA and GGA to handle strongly correlated systems is to try and localize the electrons within the orbitals. This could be important for d and f-states with low occupation, which are more localized, thus, causing problems for the LDA and GGA. This causes problems when calculating, for instance, the band gap in transition-metals [37]. One possible solution to this problem is to add Hubbard-like on-site Coulomb repulsion to the DFT functional,

$$E_{\mathrm{xc}}^{\mathrm{DFT+U}} = E_{\mathrm{xc}}^{\mathrm{DFT}} + \frac{U-J}{2}\sum_{\sigma}\left[\left(\sum_{m_1} n_{m_1,m1}^{\sigma}\right) - \left(\sum_{m_1,m_2}\hat{n}_{m_1,m2}^{\sigma}\hat{n}_{m_2,m1}^{\sigma}\right)\right], \tag{3.9}$$

by which fractional occupancy is penalized by forcing the on-site occupancy matrix $\hat{n}^{\sigma}$ towards being either fully occupied or fully unoccupied [38].

3.1.3 Solving the Kohn-Sham Equation

After choosing an exchange-correlation approximation, the more practical task of solving the Kohn-Sham equation remains. Depending on the nature of the system, the sought-after information, and the computational resources, different approaches are appropriate. For small isolated systems or molecules, one approach is to expand the Kohn-Sham orbitals in a linear combination of atomic orbitals (LCAO) [39],

$$\psi_i(\mathbf{r}) = \sum_j c_{ij}\chi_j(\mathbf{r}), \tag{3.10}$$

where $\psi_i(\mathbf{r})$ are the Kohn-Sham one-electron orbitals and $\chi_j(\mathbf{r})$ are the chosen basis set. Here, c_{ij} are coefficients determined self-consistently through minimizing the Kohn-Sham energy. This approach makes calculations considerably cheap, although the accuracy will be limited by the quality of the chosen basis. If periodic boundary conditions are applied to the system, a plane wave basis is suitable due to its inherent periodic nature. Bloch's theorem states that in a periodic potential, the wave-function has a periodic magnitude,

$$\psi_k(\mathbf{r}) = u_{\mathbf{k}}(\mathbf{r})e^{i\mathbf{k}\cdot\mathbf{r}}, \tag{3.11}$$

where $\mathbf{k}$ is the wavevector and $u_{\mathbf{k}}$ is a function with the save periodicity as the potential. Using Brillouin zone sampling [40], the wavevectors of an infinite solid can be calculated using only one unit cell, as in reciprocal space, the $\mathbf{k}$-vector is translated to k-points: sampling points in the first Brillouin zone of the material. When symmetry is applied to the system, a summation over the k-points in the irreducible part of the Brillouin zone gives the energy of the system. The number of required k-points is determined by increasing the number until convergence of a desired quantity. In material with a small bandgap, fractional occupation, or smearing of the Fermi surface, might be necessary to avoid convergence problems in the calculation caused by the finite sampling of the Brillouin zone. When applied, bands close to the Fermi energy is not as sensitive to the occupation changing throughout the self-consistent solution of the Kohn-Sham equation. The summation over the wave-functions is further truncated such that the kinetic energy of the plane waves is lower than a specified cut off energy, $\frac{\hbar^2 k^2}{2m_e} < E_{cut}$. A higher E_{cut} includes more rapidly changing features in the calculation resulting in a more accurate description of the system, but at a higher computational cost.

Treatment of Core Electrons - Pseudopotentials and PAW

Rapidly changing orbitals of the core electrons cannot in a practical manner be represented by a plane wave basis set. This problem is tackled by the use of pseudopotentials [41]. Assuming a frozen core approximation [42], in which the nucleus and innermost electrons are assumed to be unaffected by and does not contribute to chemical bonding, the pseudopotentials model the core electrons by an effective potential, treating the behavior of the core separately for that of the valence. One requirement on the potential is that it reproduces the true potential outside of the core region. The Vienna Ab initio Simulation Package (VASP) [43]–[49] (used to implement DFT in this thesis) implements the projector augmented-wave method (PAW) [50] for treatment of the core regions.

Chapter 4

From Energies to Measurable Properties

DFT provides the electronic ground state energy of the present configuration of a system. However, this lone energy does not tell us much. To draw chemical or physical conclusions about the system, the energy must be related to something.

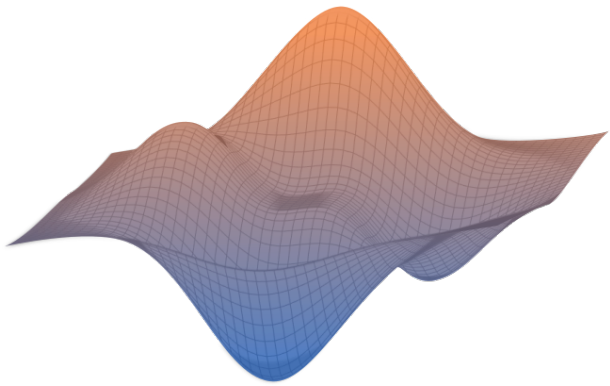

Figure 4.1: Potential energy surface.

When investigating a system, the first step is usually finding the geometric configuration, which minimizes the inter-atomic forces in the system. There are two different types of optimized structures: the local minima, being the optimal structure within a defined sub-space of the potential energy surface (PES); and the global minima, begin the most optimal geometry possible when all the PES is considered. Finding the lowest energy path for moving the system between two adjacent local minima is called a transition state search; relevant when investigating reaction mechanisms. Once a reaction mechanism has been identified, the reaction conditions must be considered. Since DFT is evaluated at zero Kelvin, the effect of temperature on the system can be considered by using ab initio thermodynamics. Further placing the optimized states (and transition states) in an experimental setting, a microkinetic model of the reaction will result in experimentally measurable quantities such as conversion and turn-over frequencies.

4.1 Local Minima Optimization

When searching for a local minimum, the goal is finding the nearest atomic structure with minimum potential energy, starting from a given initial configuration. Roughly, this is done by following the energy gradient in every coordinate direction and when the norm of the force components is below a predetermined value, the structure is considered relaxed, and the optimum geometry is found. However simple this might sound; the challenge is determining in which direction to search for the minima and reach convergence within a reasonable time.

One way of implementing a force minimization is through a steepest decent (SD) method [51]. SD follows the direction in which the forces decrease the fastest, using a set size proportional to the slope of the PES. Adding a memory of previous search direction to the method results in what is called the conjugate gradient method [52], [53]. As well as E and $\frac{\partial E}{\partial \mathbf{R}}$, the second derivative of the energy $\left(\frac{\partial^2 E}{\partial \mathbf{R}^2}\right)$ can be used for optimizing the structure, as implemented in the Newton method. When including the Hessian matrix, the optimization is faster thanks to the extended knowledge of the local curvature of the PES. However, the Hessian is, for many systems, prohibitively expensive to calculate and it is, thus, often updated from an initial guess. When the explicit Jacobian or Hessian is replaced by an approximated one, the algorithm is called a Quasi-Newton method. One method that uses curvature information to preconditioning the gradient is Broyden–Fletcher–Goldfarb–Shanno algorithm (BFGS) [54]–[58] and the limited memory Broyden-Fletcher-Goldfarb-Shanno (L-BFGS) [59]. Instead of using the Jacobian, the BFGS method updated the approximation of the Hessian from evaluation of the gradient via a finite-difference approximation of the Newton method, thus reducing the complexity of the calculation. FIRE (Fast Inertial Relaxation Engine) uses a different technique for finding the optimized structure, by introducing an acceleration in a direction that is steeper than the current direction. Combined with an adaptive time step, a time step that increases for each iteration during which convergence has not been reached, creates a method capable of finding a faraway minimum in fewer iterations [60].

When searching for a local minima convergence can be difficult to reach. However, it is possible to remove some of the degrees of freedom in the system by freezing positions, distances, bonds, or angles in the geometry. This often leads to a faster convergence, but if done carelessly, the procedure may result in a less desired geometry.

4.2 Global Minima Optimization

The PES sampled in the search for low energy structures might contain several local minima, the challenge in this case often turns into finding the local minimum with the lowest energy, i.e., the global minimum. In this search, a method for moving from one local minimum to another is needed. There are several different methods available for probing larger areas of the PES, all implement different methods for traversing the PES. However, there is no guarantee that the lowest lying minima found corresponds to the actual global minima. This must be verified outside of the optimization calculation.

4.2.1 AIMD - Ab Initio Molecular Dynamics

One such method is using the forces obtained from DFT to solve the classical Newtons laws of motion, $F = ma$. To calculate the trajectory in the simulation, the equations of motion are integrated numerically using the Verlet algorithm [61], [62]:

$$R_i(t + \Delta t) \approx 2R_i(t) - R_i(t - \Delta t) + \frac{dv_i(t)}{dt}\Delta t^2. \tag{4.1}$$

This moves the system in time and along the PES. Often, the system is given an initial energy to avoid getting stuck in a local minima. The two prevailing methods for implementing molecular dynamics in computational code is Born-Oppenheimer Molecular Dynamics (BOMD) [63] (used in this thesis) and Car-Parrinello MD (CPMD)[64]. The first propagates the ionic degrees of freedom by solving the Kohn-Sham equation at each step, the second treats the parameters describing the electronic wave function as classical degrees of freedom and propagates them as such instead of directly solving the wave function at each step.

Controlling the Temperature

AIMD simulations are either performed in the micro-canonical (keeping N, V, and T constant) or canonical (keeping N, V, and E constant) ensemble. In this thesis, the canonical ensemble is chosen, and there are several different techniques for controlling the temperature. Most of these techniques uses an external system, a heat bath, to moderate the temperature; very similarly to how an experimental setup might interact with the surrounding environment. The basic idea of all these methods is to achieve a fixed average temperature but allowing fluctuations in accordance with a canonical distribution.

Andersen's Stochastic Collisions The Andersen thermostat connects the heat bath to the studied system by use of stochastic collisions acting on randomly chosen particles [65]. The new velocities are given by the Maxwell-Boltzmann distribution for the desired temperature. However, the randomness of the assigned velocities may interrupt the dynamics of the system and thus result in a non-physical behavior.

Berendsen's Constant Scaling The Berendsen thermostat [66], which is also called a proportional thermostat, uses velocity scaling of all particles in the system to adjust the temperature. When the temperature starts to deviate too much from the desired one, all velocities are multiplied by the same factor to move the system dynamics towards the fixed average temperature. This method minimizes the local interference of the temperature adjustment. However, the constant scaling of all velocities at once does not always result in a true physical behaviour [67].

Nosé-Hoover's Friction Moderation This thesis utilizes the Nosé-Hoover [68], [69] thermostat, in which the heat bath is introduced as an additional degree of freedom in the Hamiltonian of the system. The heat bath will work like friction, slowing down and speeding up the particles in the system, such that the electronic response moves the

system towards the desired temperature. This method introduces the inherent energy fluctuations of a system with temperature, thus the coupling between the heat bath and the system must be chosen carefully for the process to work. If the coupling is too loose the temperature control will be poor and if it is too tight the system temperature will start to oscillate.

4.2.2 Simulating Annealing

When starting from an arbitrary structure, the search for the global optimum always runs the risk of getting stuck in a local minimum. One way to minimize this risk is to create the effect of annealing by changing the temperature of the MD calculation. The temperature added to the system is then in a first phase increased, so as to leave a potential local minimum, and then decreased to allow the structure to settle into a more optimized structure. Care must be taken to avoid increasing the temperature too rapidly, lest the temperature distribution become uneven, creating unphysical motion for single atoms.

4.2.3 Basin-Hopping

A different way of moving between the local minima on the PES is implemented in the Basin-hopping routine. Where one possible implementation is based on three steps: random perturbation of coordinates, local minimization of the new configuration, and acceptance or rejection of the new structure based on the minimized value of the structure [70]. How to determine which structures are accepted might differ between implementations. One way could be to always accept structures of lower energy than the last and accepting structures of higher energy with a certain probability, i.e., following a Monte Carlo sampling approach. Here the energy required to move from one structure to another is irrelevant; there is no threshold to overcome since the new structures are random. However, the random displacement limits the search of the PES. Figure 4.2 shows the result of applying a basin-hopping routine to optimizing small clusters of different elements.

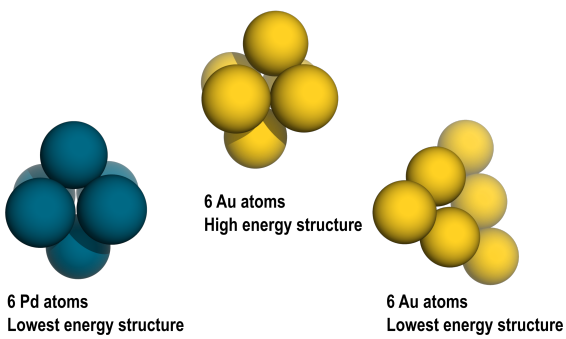

Figure 4.2: In a high-dimensional space the basin-hopping method is appropriate. One application is optimizing the structure of clusters.

4.3 Transition State Search

Moving along the PES and jumping between local minima configurations means crossing an energy barrier as the energy between the sites, by definition, is higher than those of the minima. On a realistic PES, there might be several different paths between two minima. The top of the barrier is a saddle point called a transition state (TS). These saddle points are local maxima only in the direction in which the transition occurs; in all other directions it is a local minimum. To find these reaction paths, methods utilizing the first order derivative of the PES are employed. Often it is the reaction path with the lowest TS energy that dominates the kinetics of the system.

The Nudge Elastic Band Method

As the method name suggests, the idea behind the Nudge Elastic Band method (NEB) [71], [72] is to attach an elastic band to the initial and final state of the reaction and, tightening the band, forcing it down to the lowest energy path between the states. To determine what this path looks like, intermediate equidistant states are connected with springs along the band and optimized both on spring force and potential energy. The distance between the intermediate states might result in missing the actual position and the exact energy of the saddle point, even though the path is found. In addition to the standard NEB there is a climbing-NEB method which allows the intermediate state closest to the saddle point to climb to the top of the barrier, thereby capturing the energy of the actual transition state [73], as illustrated in fig. 4.3. NEB must be supplied with an initial and a final state. NEB also needs a starting guess of the path, often provided by an interpolation between the two given states [74]. The method will only find the TS closest to the starting guess, i.e., a different starting guess might result in a different TS.

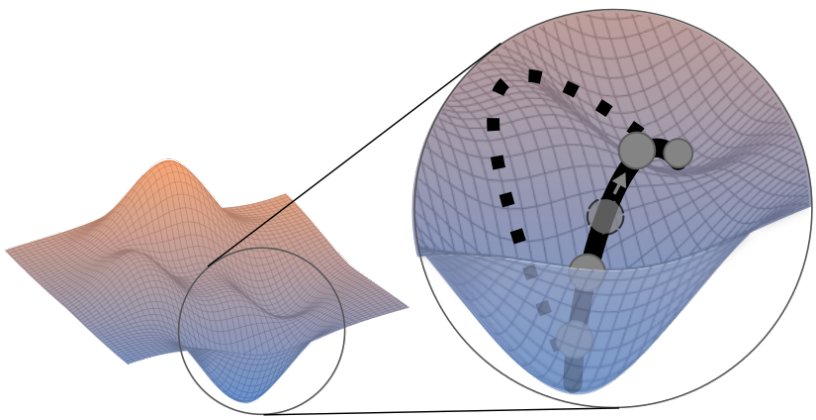

Figure 4.3: To identify the lowest energy path between two local minima, the NEB method will use a starting interpolation (dashed line) and find a lower energy path (solid line). When applying the climb option, one image will climb to the top of the band, making sure the transition state is captured.

The Dimer Method

If the end state of the transition is unknown or for another reason not available, the Dimer method [75] is a transition state tool that only requires an initial state. The Dimer method connects two images by a vector and rotates the second image around the starting guess to find the direction for which the gradient of the vector is the smallest. The procedure is repeated until a first-order saddle point is reached.

These two TS-methods, NEB and Dimer, can be used both individually and concurrently.

4.3.1 Molecular Vibrations

A non-linear molecule of N atoms has 3N degrees of freedom corresponding to translations, rotations, and vibrations. 3N-6 of these are normal modes of vibration, the 6 degrees of freedom removed being those of translation and rotation in 3 dimensions (a linear molecule has 3N-5 degrees of freedom since rotation along the axis of the molecule has an infinite symmetry number). The vibrations are oscillations around the equilibrium structure found by a geometry optimization. The composition and character of the bonds determine the vibrational frequencies, which becomes an identifying characteristic of the molecule.

When calculating the vibrational frequencies, all natural frequencies related to movements in space (i.e., translations and rotations) will be (close to) zero. For a transition state, the configuration is not at a local minimum, and is thus possible to displace along the reaction path. Depending on the shape of the TS, one or more of the vibrational degrees of freedom will then be characterized by imaginary frequencies.

4.4 Ab Initio Thermodynamics

Standard DFT yields the ground-state properties at zero-temperature conditions. In contrast, experiments are performed at elevated temperature and in the presence of reacting gases. To account for a more realistic environment, DFT can be used together with thermodynamics.

Relative Stability of Different Structures

To compare the relative stability of different systems the total energy of the combined systems must be known, along with the energy of the components. Adding atoms to a system means taking them from a reservoir, the cost of using the reservoir can be accounted for in terms of their chemical potential. The standard chemical potential, or standard free energy, [76] is given by,

$$\mu^0(T) = -k_B T \ln \left[\left(\frac{2\pi m k_B T}{h^2} \right)^{3/2} k_B T \right], \tag{4.2}$$

where k_B is Boltzmann's constant, T is the temperature, m is the mass of the atom comprising the gas, and h is Planck's constant. To calculate the maximum of reversible

work that can take place in the NVT ensemble under a given set of environmental conditions, the change in Gibbs free energy, ΔG (at a fixed temperature T) is calculated according to

$$\Delta G = \Delta H - T\Delta S, \tag{4.3}$$

where ΔH is the change in enthalpy and ΔS is the change in entropy. When a system reaches equilibrium at constant pressure and temperature, this available free energy, is minimized [77]. When comparing systems where the number of constituents or the included species change, the Gibbs free energy of formation must include the change in chemical potential,

$$\Delta G^{form} = \Delta H - T\Delta S - \Delta\mu. \tag{4.4}$$

In this thesis, the change in enthalpy is approximated as the relative total energy of formation [78], and is given by

$$\Delta H \approx \Delta E^{form} = E_{A+B} - E_A - E_B, \tag{4.5}$$

where E_{A+B} is the energy of the total system, E_{rA} the energy of system A, and E_B the energy of system B. ΔS in eq. (4.4) is the difference in entropy between system $A + B$ and system A,

$$\Delta S = S_{A+B} - S_A, \tag{4.6}$$

while the entropy of system B, the chemical potential, is calculated in relation to a chosen reference pressure

$$\Delta\mu(T, p) = \mu^o(T, p^o) + k_B T \ln\left(\frac{p}{p_o}\right). \tag{4.7}$$

To calculate the entropies in eq. (4.6), the partition function of the systems must be known and, thus, the vibrational frequencies of the relevant species calculated. In this thesis, the translational degrees of freedom were calculated using the ideal gas approximation, whereas their vibrations, along with the vibrations of the zeolite systems, were approximated as harmonic oscillators as per the implementation in the Atomic Simulation Environment (ASE) [79], [80].

4.5 Reaction Kinetics

One of the purposes of using a catalyst is to divert a reaction into a new, more energetically favorable path, thereby increasing the rate of the reaction. This new catalyzed reaction path is identified using the tools introduced previously in this chapter, resulting in a reaction mechanism with the characteristics of that in fig. 2.1. Connecting the identified reaction to experimentally measurable conversion and selectivity, can be done through kinetic modeling. The first step in kinetic modeling is to calculate the rate of the elementary reaction.

4.5.1 Time evolution of the reaction

To get the time evolution of the system, a master equation [81] is used. In this context, all reaction intermediates and TSs are referred to as *states*, and the master equation

describes the changing probability of finding the system in a given state. Written in the form

$$\frac{d\mathcal{P}_\alpha}{dt} = \sum_\beta \left(W_{\beta\alpha}\mathcal{P}_\alpha - W_{\alpha\beta}\mathcal{P}_\beta\right), \tag{4.8}$$

the equation gives the change in probability of finding the system in state α, where $W_{\beta\alpha}$ is the transition rate from state β to state α and $\mathcal{P}_\alpha$ is the probability of finding the system in state α. The sum over β account for all paths to α.

Mean-Field Approximation

In a system of single-site catalysts, the distance between the active sites implies no interaction between different sites and for a sufficiently large number of sites, a mean-field approximation [5] (additionally assuming an even and random distribution of the reactants) should be acceptable. With this approximation, the probability of being in state α is the average concentration of α.

Transition State Theory (TST)

To calculate the rate for a transition, i.e. $W_{\beta\alpha}$ or $W_{\alpha\beta}$ in eq. (4.8), rate constants are estimated using transition state theory (TST) [82]. Moving from the reactant R, through the activated transition state $R^\ddagger$ to the product state P, can be visualized as

$$R \rightleftharpoons R^\ddagger \rightarrow P. \tag{4.9}$$

In TST, recrossing the barrier is not allowed, hence the one way arrow between $R^\ddagger$ and P. However, the back reaction is gained from letting R and P switch places. From this, the rate at which a given reaction occurs is given by the probability of being in the TS compared to that of being in the reactant state, times the *trial frequency* f,

$$W_{\beta\alpha} = f\frac{\mathcal{P}(R^\ddagger)}{\mathcal{P}(R)} = f\frac{Z^\ddagger}{Z}. \tag{4.10}$$

The trial frequency is generally considered to be the vibration along the reaction coordinate, i.e., the vibration crossing the TS. The second identity in eq. (4.10) comes from the mean field approximation, equating the probability of being in a state with the partition function of that particular state. Assuming that the system follows the Boltzmann distribution and that the trial frequency is low ($k_BT >> hf$), and relating the energy of the TS to that of the reactant, the rate becomes

$$W_{\beta\alpha} = \frac{k_BT}{h}\frac{Z'^\ddagger}{Z}e^{\frac{-\Delta E}{k_BT}} = k_{TST}, \tag{4.11}$$

where ΔE is the energy difference between the two states, and $Z'^\ddagger$ and Z are the partition functions with reference to the local energy minima. The reaction coordinate has been excluded in $Z'^\ddagger$. k_{TST} is the transition state rate constant.

In steady-state, the time derivative of the rate in eq. (4.8) equals zero. For a closed system, this implies an equilibrium between the reactants and the product.

Chapter 5

Methane to methanol conversion

Approximately 82% of the energy used today comes from fossil resources [83], of which 32% is oil, 26% is coal, and 24% is natural gas. Out of these, coal is the easiest to manage. Its solid form makes it easy to handle, and it is neither explosive nor poisonous. Oil is somewhat more difficult to manage as it is liquid at room temperature. The fumes exuded from gasoline are toxic carcinogens, potentially causing respiratory failure, fatal arrhythmia, and even death. In addition, contact to the skin is harmful and may cause chemical burns [84]. Despite the health risks, the infrastructure for managing and transporting liquid fuels is extensively developed and makes oil accessible worldwide. The most difficult to manage of the fossil energy sources is natural gas. Colorless and practically odorless, it is explosive, and though not poisonous, it can replace oxygen in the lungs causing suffocation [85]. Thus, care must be taken to ensure that transportation, storage, distribution, and use of natural gas are safe, resulting in less extensive networks of natural gas pipelines. Out of the three fossil energy sources, natural gas is the cleanest.

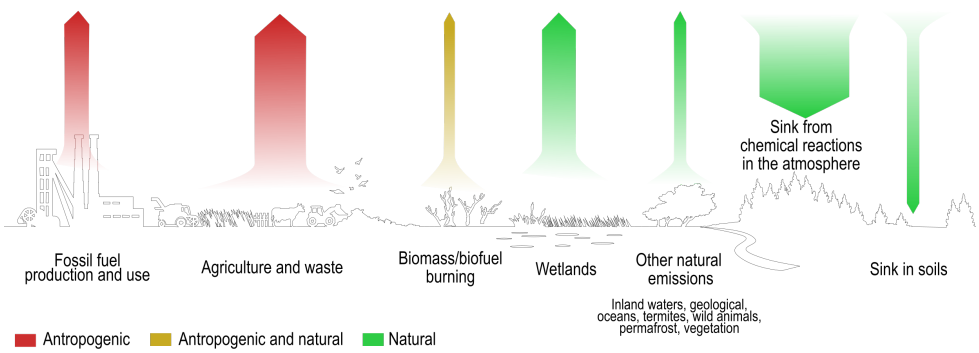

Figure 5.1: Methane sources and cycle. Methane is released into the atmosphere from industrial and biological sources, while sinks are provided by chemical reactions in the atmosphere and soil deposits. Due to industrial emissions, more methane is released than captured [86].

It emits fewer air pollutants to the environment when combusted as compared to both coal and oil, along with 40% and 20% less CO_2 than coal and oil, respectively [87]. In addition, the main component in natural gas also occurs in a non-fossil form as biogas, or biomethane. Produced by anaerobic digestion of organic matter, this fuel has a zero net emission through its life cycle, and as a renewable natural gas it is indistinguishable from fossil natural gas in its composition and utilization [88].

To ease the handling and transport of natural gas, liquefaction is often used [89]. Kept at 20–25 MPa or -163 °C, the liquefied gas becomes less space-consuming and more manageable to transport. However, before use, it must be regasified, again becoming volatile. A more practical alternative to liquefaction is the chemical conversion into a substance that is in liquid form at room temperature, thus reducing the need for temperature/pressure control during transport. Preferably this substance should be directly usable as an energy source, eliminating the problems of managing gaseous fuels. One such conversion could be converting the main ingredient in natural gas, methane, into methanol. As a fuel, methanol can be used as a direct replacement of gasoline, and (with modifications to the engine) as a replacement for diesel. It emits less NO_x and sulfur species than traditional fuels, and the energy efficiency is as high or even higher when running an engine on methanol as compared to traditional liquid fossil fuels [90]. One drawback of alcohol fuels is their energy content. Methanol has approximately half the energy content of diesel, and thus more fuel is required [90]. Like oil, methanol has adverse health effects on humans as both fumes and liquid are toxic when inhaled or ingested, which can, e.g., cause blindness, but potentially also nervous system depression, coma, and death, at high enough exposure. Dermal contact is substantially less harmful, causing at most dermatitis as methanol defats the skin [91].

Preferably, the conversion from gaseous to liquid fuel would be done at the extraction site. However, this is not realistically possible with the technology available today. Converting methane into methanol is currently a highly energy-demanding, multiple-step process, only economically feasible at large power plants. This is in stark contrast to the often remote and isolated natural gas and oil extraction sites.

5.1 Multi-step conversion

The industrial transformation of methane to methanol has a history starting in 1923. The process of steam reforming is done in 9 steps: dissociating each of the hydrogen from the methane (4 steps), dissociating water (2 steps), and finally forming carbon monoxide and hydrogen on the catalyst surface (2+1 steps). Overall, the process of steam reforming,

$$CH_4 + H_2O \rightleftharpoons CO + 3H_2 \qquad \Delta H = 2.15 \text{ eV}, \tag{5.1}$$

is an endothermic reaction, and together with the water-gas shift reaction,

$$CO + H_2O \rightleftharpoons CO_2 + H_2 \qquad \Delta H = -0.43 \text{ eV}, \tag{5.2}$$

synthetic gas, or syngas, is formed. The steam reforming is performed over Ni particles dispersed on an Al_2O_3 or $AlMgO_4$ spinel. Other transitions metals are also able to catalyze the reaction, but Ni is the more economically feasible. As the reaction is endothermic, it is highly energy-intensive and performed in conditions of up to 1200 K and moderate pressures (25-35 bar). The heat for the reaction is, for instance, supplied by direct combustion of some of the methane supplied to the reaction. In this scenario, methane is fully oxidized into syngas (CO, CO_2, and H_2), and then reassembled into methanol or other hydrocarbons. Today, the formation of methanol from syngas is performed

over a $Cu/ZnO/Al_2O_3$ catalyst operated at 50-100 bar and 500-550 K [5]. Including the eight steps of the water-gas shift reaction, the formation of methanol passes through 13 elementary reaction steps to hydrogenate all hydrocarbon species before forming CH_3OH. Overall, the methanol formation reaction can be written as:

$$CO + 2H_2 \rightleftharpoons CH_3OH \qquad \Delta H = -0.95 \text{ eV}, \tag{5.3}$$

or rather,

$$CO_2 + 3H_2 \rightleftharpoons CH_3OH + H_2O \qquad \Delta H = -0.49 \text{ eV}, \tag{5.4}$$

depending on the fractional composition of the gas supplied to the reactor [92]. In modern plants, the exothermic methanol synthesis is utilized in the endothermic steam reforming. This two-stepped, coupled procedure requires industrial-scale production with large power plants to be economically viable. A schematic layout of the reactor process can be found in fig. 5.2.

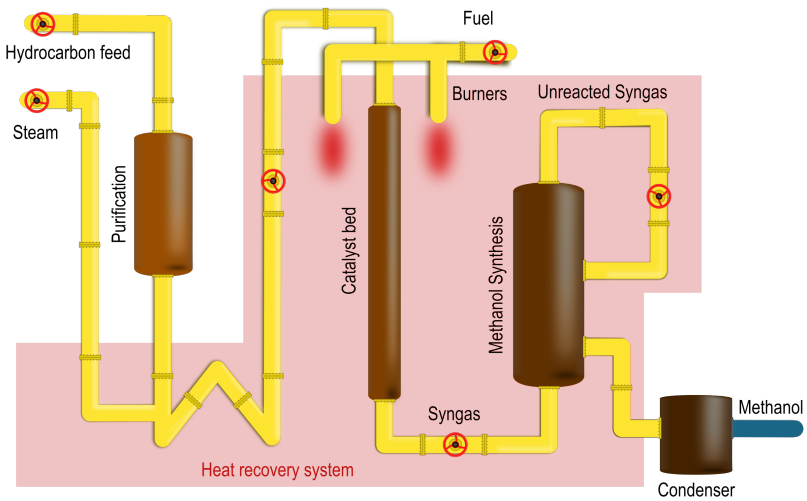

Figure 5.2: A combined steam reforming and methanol formation reaction process.

Catalysts containing copper are sensitive to site blocking poisons, such as sulfur which may cause complete deactivation of the catalyst. The catalyst must also be protected from sintering by, for instance, maintaining a temperature below 575 K and reducing chlorine compounds. In addition, the presence of liquid water may lead to a more rapid growth of copper crystals, destroying the catalyst matrix. This results in an average industrial lifetime of 2-5 years for the catalyst [93]. The selectivity toward methanol over the $Cu/ZnO/Al_2O_3$ catalyst is >99.5%. It is the Cu crystallites that have been identified as the active sites for the reaction (though the absolute state of the site is still under debate), while the interaction between ZnO and the supporting Al_2O_3 is believed to reduce the potential for DME formation, thus increasing the selectivity towards CH_3OH

[93]. The $Cu/ZnO/Al_2O_3$ catalyst have, for a pressure of 50 bar and 513 K, shown a TOF of $1.6 \cdot 10^{-2}$ s^{-1} per site [94]. Behrens et al. [95] found a similar activity with $2.1 \cdot 10^{-2}$ s^{-1} per site for their intrinsically most active sample. Pure Cu reference surfaces have shown similar results, indicating the activity of the copper in $Cu/ZnO/Al_2O_3$. The pure Cu(100) surface have shown a TOF of $2.7 \cdot 10^{-4}$ s^{-1} per site, with an apparent activation energy of 69 ± 4 kJ mol^{-1} at 543 K [96], while Cu(110) have shown a TOF of $6 \cdot 10^{-3}$ s^{-1} per site at 510 K and 51 bar [97].

5.2 Direct conversion

The massive scale needed to make the traditional conversion of methane (via syngas) to methanol puts limits on its application. In addition, the complex reaction path and intricate reactor design needed to optimize the energy-intensive process, makes the multi-step process vulnerable to shutdowns, during which the methane meant for conversion is vented or flared. To enable more widespread, reliable, decentralized methane conversion, the reaction must be enabled at ambient temperature and pressure. In principle, it is possible to perform small scale, low temperature, direct conversion of methane into methanol:

$$CH_4 + \frac{1}{2}O_2 \rightleftharpoons CH_3OH \qquad \Delta H = -1.32 \text{ eV}.$$

Unfortunately, utilization of this reaction requires a catalytic material not yet identified. Finding a catalyst with a high selectivity towards partial oxidation of methane is difficult due to the high stability of the methane molecule. The energy required to break the first carbon-hydrogen bond makes it difficult to stop the complete oxidation, thus often resulting in thermodynamically favored competing reactions,

$$CH_4 + \frac{3}{2}O_2 \rightleftharpoons CO + 2H_2O \qquad \Delta H = -5.41 \text{ eV},$$

$$CH_4 + 2O_2 \rightleftharpoons CO_2 + 2H_2O \qquad \Delta H = -8.26 \text{ eV},$$

as utilized in the water-gas shift reaction. However, there are reported catalysts able to do the partial oxidation reaction, though these typically exhibit either low selectivity, or high selectivity but low activity. One example of a very selective biocatalyst is enzymatic methane monooxygenases (MMOs) [99], [100]. In the MMO, the active sites are spares metal atom sites (fig. 5.3); the membrane-bound enzyme pMMO enables partial oxidation of methane over its isolated copper atoms, while the enzyme in its soluble form (sMMO) performs the reaction over iron dimer active sites using O_2 as the oxidant [101]. The conversion over the active sites is performed with a very high selectivity, but (for industrial use) too low activity. To mimic this very selective process, metal ion-exchanged zeolites are of interest. The availability of different porosity of the zeolite frameworks, the possibility of isolated active sites, and the diversity in the characteristics of the structures make them promising catalytic materials. Based on the MMO structures (see fig. 5.3), the composition of the active site is possibly based on Fe and Cu, and thus, other transition metals might also be of interest. The structure of the active site in the zeolite is an

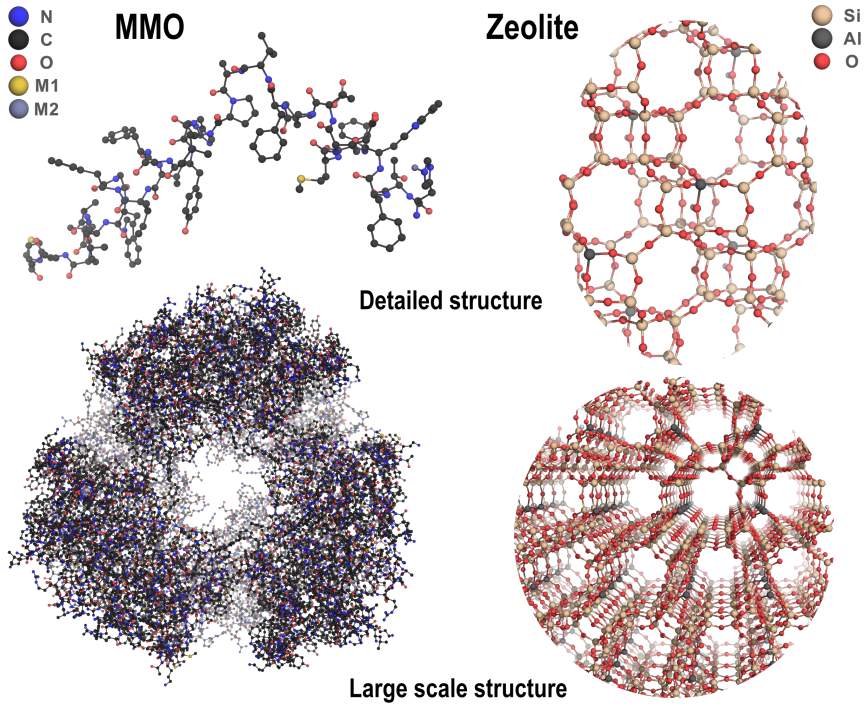

Figure 5.3: The protein responsible for oxidation of methane in nature, MMO [98], alongside the zeolite structure of SSZ-13. The structures are similar, both on a small and a large scale, having a porous structure and the possibility of single, metal atom sites. MMO is composed of carbon, nitrogen, oxygen, and sparse metal sites (here denoted M1 and M2); the components of the zeolites are silicon, aluminum, oxygen, and the possibility of charge compensating metal sites.

extensively investigated topic; the most prevalent site structure and its distribution is affected by the pore size, cage size, and general structure of the framework, together with Si/Al ratio, and Al-Al distance. As a result, different zeolite structures appear to stabilize different sizes for the active site. The structures with larger pores (e.g. MFI, MOR) exhibit the existence of trimer structures [102], while small-pore zeolites (e.g. CHA) predominantly supports monomers [103] and dimers [104]. This is not to say that the most prevalent site is necessarily the most active structure in the framework. The internal conditions of the zeolite are important to the activity, the active site structure, as well as the reaction conditions. As the zeolite is very humid, the presence of water must be accounted for as it affects the composition of the zeolite cage [105], the oxidation of the active site [106], [107], and the mechanism for methane to methanol conversion [108], [109]. The activity of the zeolite has been shown to depend heavily on its water content, possibly affecting the mobility of the atoms in the active site, changing barriers and desorption energies [110].

As of yet, it has proven difficult to performed a continuous reaction cycle over the zeolite, and as a result, the most common experimental procedure is a quasi-catalytic cycle divided into three parts (fig. 5.4): activation of the oxidant (typically O_2, N_2O, NO, or H_2O_2) over the active site at high temperature (>623 K); reaction phase at 323–483 K and with addition of CH_4; extraction at 278–483 K, where products are flushed out using water/ethanol or some other solvent [111]. The main reason for the change in reaction conditions during the reaction cycle is the need to reactivate the active site as the reaction itself deactivates the system, and the difficulty in removing the products, leading to the catalyst being poisoned by CH_3OH.

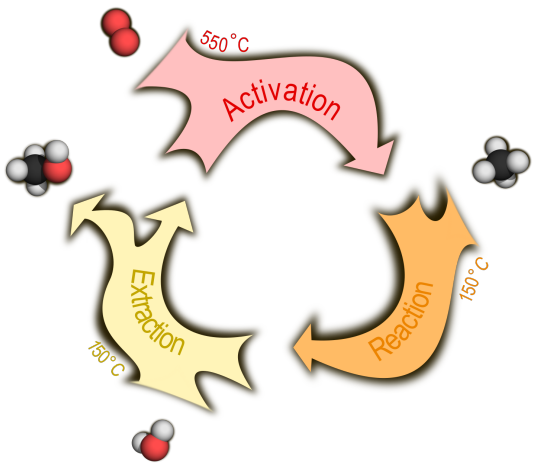

Figure 5.4: Reaction conditions for the quasi-catalytic reaction cycle over zeolites for direct methane to methanol conversion. The three steps in the reaction are necessary to first activate the system and to extract the products.

Using this three step method, the small pore zeolite Cu-SSZ-13 has been shown to yield 28–31 $\mu\text{mol}_{CH_3OH} g_{cat}^{-1}$, where the lower yield corresponds to a lower Si/Al ratio (Si/Al=6 and 12, respectively) in the zeolite [112], however the selectivity of the conversion is not reported. The Cu-ZSM-5 has shown a selectivity of 98% towards methanol, unfortunately the yield was mush lower at 8.2 $\mu\text{mol}_{CH_3OH} h^{-1} g_{cat}^{-1}$ [113] with Si/Al = 12. A slightly higher value of 18.6 μmol_{CH_3OH} h^{-1} g_{cat} was found for Cu-ZSM-5 with an Si/Al = 6.5 [114]. Notably, the reported yield might depend on the extraction method and solvent used [112]. Recently, it has also been shown that conversion can be achieved in a continuous manner, where after pretreating the catalyst at a high temperature (∼800 K), the reaction is performed continuously at ∼500 K [115], where Na-SSZ-13 has been reported to produce 3.12 ± 0.01 $\mu\text{mol}_{CH_3OH} h^{-1} g_{cat}^{-1}$ [116]. Using the same methodology, the large pore, channel containing zeolite H-ZSM-5 shows a yield of 1.79 ± 0.02 μmol_{CH_3OH} h^{-1} g_{cat}. A selectivity of 100% have been reached over Fe-ZSM-5 (using N_2O as oxidant) with a yield of 18–21 μmol_{CH_3OH} g_{cat} [117], and over Co-ZSM-5 (using air as oxidant) with a yield of 0.3 μmol_{CH_3OH} g_{cat} [118].

It is clear that the zeolites are able to catalyze the partial oxidation of methane. However, there is a debate as to what active site, and what zeolite structure, is responsible for the highest activity, and selectivity. As indicated by pMMO, copper seems to be one of the most promising candidates for the reaction over ion-exchanged zeolites. Several structures have been suggested as responsible for the conversion, such as: Cu_2O in MOR [119], Cu_2O in ZSM-5 [120], Cu_2O_2 and Cu_2O in SSZ-13 and SSZ-39 [121], Cu_2O_2 in ZSM-5 [122], and Cu_3O_3 in MOR [123]. Active sites composed of iron, Fe_2O_2 in ZSM-5 [117], and cobalt, CoO and Co_3O_4 in ZSM-5 [118], have also been suggested. The formation and specific function of the active site is also under debate. A proposed mechanism for the formation of the Cu_2O and Cu_2O structures is via a CuOH intermediate [121], where an intermediate CuO structure is also proposed to be promoting CH_4 conversion [124]. Over Cu-SSZ-13, the Cu_2O structure is proposed as an active site structure showing selectivity towards methane formation, while other Cu structures and Cu_xO_y clusters promote complete CH_4 oxidation to CO_2 [115]. The selectivity towards methanol is suggested to not only depend on the structure and composition of the active site, but also on the Si/Al ratio of the zeolite framework [121], with a ratio of Si/Al$\approx$ 12 being preferred in the CHA structures. With all these proposed sites and functions, it is still left to explore the detailed mechanisms of the active site formation and partial oxidation over the sites in the specific framework.

5.3 Functionalized zeolites for partial oxidation of methane

The most promising active site based on prevalence and yield is the copper dimer structure. In the large-pore zeolite Cu-ZSM-5, the selectivity has proven very good, but the yield is low [113]. This contrasts with the small-pore Cu-SSZ-13, in which the yield is considerably higher [112]. Both the Cu-ZSM-5 and Cu-SSZ-13 have been shown to contain the Cu dimer structure; however, no fully catalytic mechanism has been identified over the sites.

To investigate the activity of a potentially catalytic system, the steps presented in fig. 5.5 has been used. With DFT as the basis, these methods were used to form a coherent picture of the structure and properties of the zeolite system, with the aim of ultimately evaluating its suitability as a catalyst for the partial oxidation of methane, and to indicate elements and areas of interest for future investigation. Firstly, DFT was used to study the elementary processes involved in partial methane oxidation. This includes the interaction between methane, both as a whole and its dissociated fragments, and the active site in the zeolite. A global optimization of the structures was required as the PES of the zeolite is very flat. Thus, MD was implemented in a fashion to simulate annealing of the system. A local optimization of the lowest energy structures produced by the MD run was then performed. All the intermediate states of the reaction mechanisms were identified using this technique. The barriers of the mechanism were identified using the NEB method with the additional climbing option. Secondly, a detailed microkinetic model was built for the partial oxidation of methane over the zeolite, providing a more fundamental understanding of experimental data. Lastly, to assess the validity of the results and the models used for the calculation, the calculated reaction rate, apparent activation energies, TOF, and coverages can be compared to experimental data.

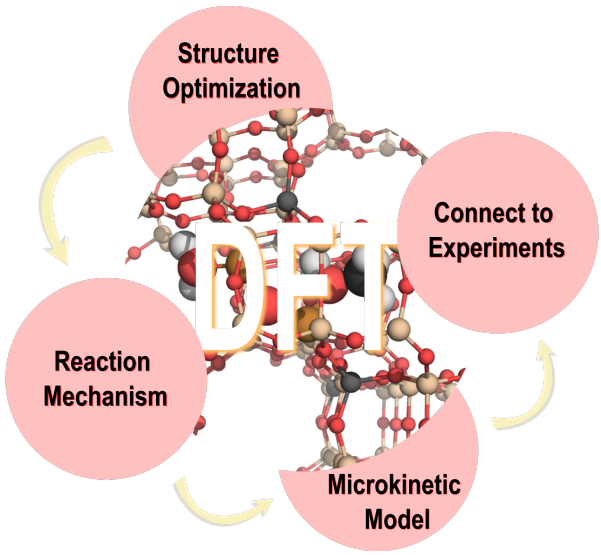

Figure 5.5: Schematic view over the steps used in this thesis to study the direct conversion of methane to methanol.

To design a functional catalyst, it is essential to know what the material looks like during reaction conditions, as well as how the reaction proceeds over the present active sites of the catalytic material. The first step is to determine how the experimental conditions of the activation and extraction phase affect the Cu_2 motif (**Paper I**). Comparing different $Cu_2O_xH_y$ structures during relevant temperature and pressure of O_2 and H_2O reveals the thermodynamic stability of different structures and compositions. The thermodynamic preferred motifs are not necessarily the most active; to investigate the activity of the identified sites, the reaction mechanism for direct methane to methanol conversion is identified and a microkinetic model is used to explore the activity of the reaction (**Paper II**). To account for the inherent humidity of the zeolite, two mechanisms are investigated, one dry and one where water is added to the mechanism and allowed to interact with the intermediates. After concluding whether the active site can catalyze the desired reaction or not, a fully catalytic reaction mechanism is identified over the relevant active site structures. Again, one dry and one wet reaction path is investigated to elucidate the effect water has on the reaction. Both the dry and the wet mechanisms must recreate the initial structure of the active site, forming a closed cycle, and preferably there should not be a need for a change in conditions during the complete cycle. Again, the activity of the mechanism is explored using a microkinetic model (**Paper III**). Having identified an active site structure and a mechanism capable of performing the desired task, one might investigate whether the identified structures and mechanisms are suitable for other metal compositions of the active site. In **Paper IV**, Cu is exchanged for other transition metal atoms and transitions metal alloys to investigate the viability of other active site compositions for the identified reaction mechanism.

Model imitations and conventions

In this thesis, several limitations have been set to the structure of the zeolite. All calculations have been performed with one Si/Al and Cu/Al ratio. The Al is chosen to create the zeolite framework, however, changing acidity of the silica framework is one further way of changing its functionality. The smallest and second smallest unit cell is chosen for the calculation; thus, the possible interactions of the reactants over the unit cell cannot be excluded. Further, all ion-exchanged sites in the zeolite are identical and the possible interaction between different active site structures, and the possible role of different active sites in the same reaction mechanism is not investigated. The possible presence and function of Brønstedt sites are also excluded. In addition to the limitation to the active site, the diffusion of the reactants and products inside the zeolite is also neglected, thus somewhat ignoring the importance of the zeolite's function as a sieve.

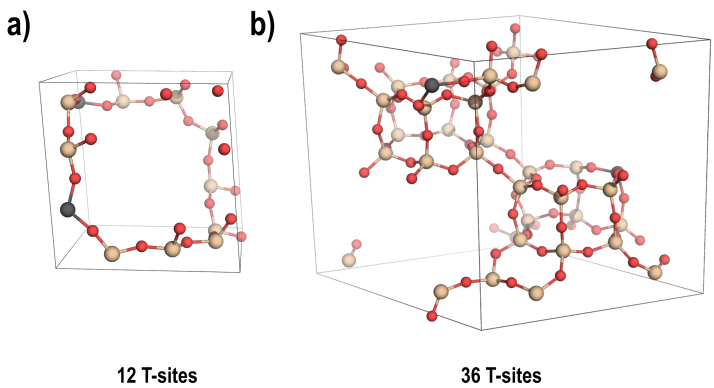

Figure 5.6: Unit cells chosen for each of the papers. a) 12 T-sites unit cell, used in **Paper I** and **Paper II**. b) 36 T-sites unit cell, **Paper III** and **Paper IV**.

In **Paper I** and **Paper II**, the SSZ-13 was modeled using the small unit sell of 12 T-sites and an Si/Al ratio of 5 (fig. 5.6a)), while in **Paper III** and **Paper IV** the unit cell with 36 T-sites and Si/Al=18 was used (fig. 5.6b)). The positions of the aluminum atoms were chosen as the most energetically favorable positions while also adhering to Löwenstein's rule. Löwenstein's rule states that two AlO_4-tetrahedrons are not allowed to share an oxygen bond [125]. In each of the unit cells, the optimum Al position is in the 8MR, separated by 2 Si tetrahedron. To compensate for the introduced charge, one copper for each aluminum was added to the system. Thus, this $Z_2[Cu_2]$ motif formed the initial configuration of the active site. The notation Z_2 is here chosen to emphasize that there are 2 Al atoms in each unit cell of the SSZ-13 framework. The $Z_2[Cu_2]$ motifs, (fig. 5.6), are chosen as the references for the calculations.

In the reaction mechanisms (**Paper II**, **Paper III**, and **Paper IV**), two different notations are used. During the activation phase, the notation is chosen to emphasize the structure of the metal ions of the active site. During the reaction and extraction phases, the two metal ions of the active site are located in the 8MR and denoted as *. Hence,

*X,Y implies that reaction intermediate X is coordinated to the metal ions, forming the current state of the active site, while reaction intermediate Y is either adsorbed on the active site or free in the zeolite.

The reaction landscape was evaluated using three different exchange-correlation functionals. The GGA as implemented by Perdew–Burke–Ernzerhof (PBE) [26] is used to describe local and semi-local exchange–correlation effects. One approach to include vdW-interaction is by using a nonlocal correlation term in the exchange–correlation functional (vdW-DF) [32], [33], [126], [127], using consistent-exchange gives the functional vdW-DF-cx [128]. The Bayesian error estimation functional (BEEF) [129] is a semi-empirical density functional developed by fitting experimental data for molecules, surfaces and bulk materials [130], that also includes vdW-interactions. To account for the highly localized 3d-electrons of oxidized copper, the functionals are also used together with a Hubbard term (+U). The U-parameter for Cu 3d is set to 6 eV as proposed by Isseroff et al. [131]. Figure 5.7 shows the partial oxidation reaction over $Z_2[Cu_2O]$, calculated using the three exchange-correlation functionals with and without the Hubbard term.

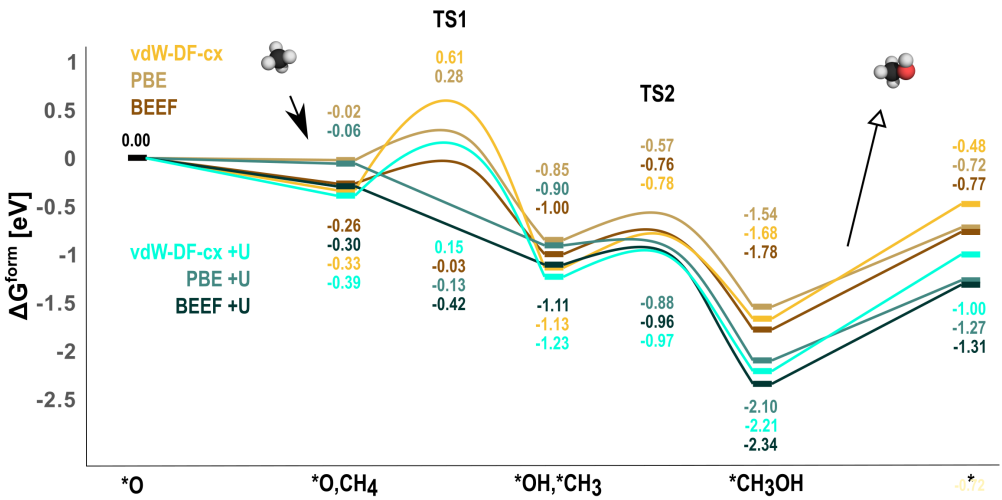

Figure 5.7: Three different functionals, with and without a Hubbard term, has been evaluated for the calculations.

In the inclusion of CH_4 into the cage, the importance of including the van der Waals interaction is noticeable, as BEEF and vdW-DF-cx both account for the introduction of CH_4, while PBE does not. The +U contribution influences the stability of the intermediate states. However, as the reaction mechanism is used to calculate the TOF of the reaction, the effect of the lowered barriers and stronger bound intermediate states will cancel, having only a minor impact on the rate of the reaction.

5.3.1 Cu-dimer motifs during reaction conditions (Paper I)

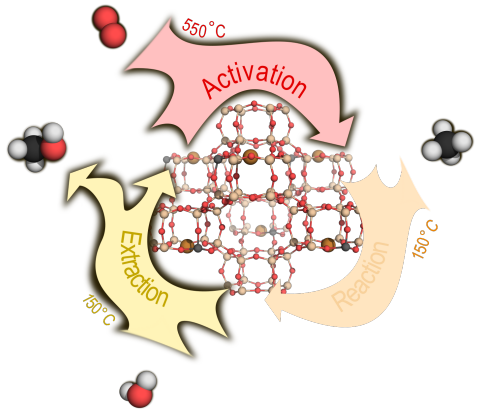

Figure 5.8: In **Paper I**, the stability of different Cu_2-cluster structures were investigated during the reaction conditions of activation and extraction for direct methane to methanol conversion.

The motif of the Cu-dimer was investigated during conditions of activation (848 K, 20% O_2, 10^{-8}% H_2O) and extraction (448 K, 4% H_2O, 10^{-8}% O_2) (fig. 5 .8)[132]. The $Cu_2O_xH_y$ structure is always situated in the 8MR of the zeolite framework, while the atoms of the reference Cu_2 is located in 6MRs; the barriers for forming the Cu clusters are not taken into account. The formation energy of the Cu_2 motifs can be seen in fig. 5.9.

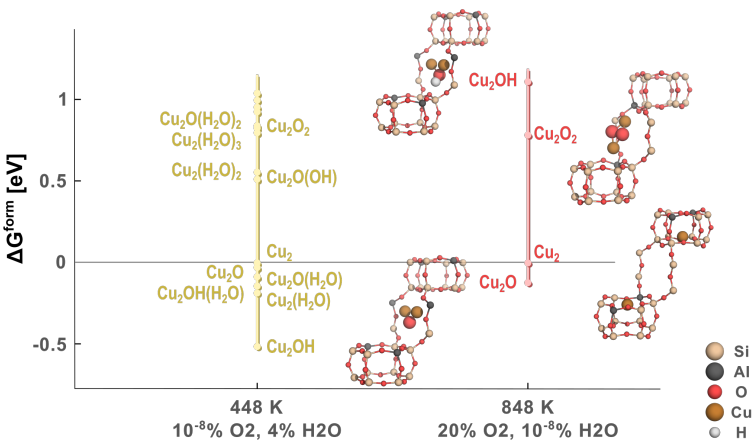

Figure 5.9: All investigated structures displaying a formation energies below 1 eV at reaction conditions. Included structures are the motifs present at both reaction temperatures.

At activation conditions, all moisture in the clusters has been removed, and there are only two stable active site structures, the reference structure Cu_2, and Cu_2O. At a formation energy of 0.78 eV Cu_2O_2 is found, and at 1.11 eV Cu_2OH is formed. At the lower temperature, conditions of extraction, there are several stable cluster structures, all including OH of H_2O, except Cu_2 and Cu_2O. The most stable structure is Cu_2OH with a formation energy of -0.52 eV.

The stability of the structures over a range of temperatures and O_2 pressures is shown in the phase diagram of fig. 5.10. It is found that the stable state is dependent on temperature and pressure, as well as the starting configuration of the site. A structure formed from the already oxidized Cu_2O will, in general, be more stable than one formed from Cu_2. The Cu_2O site also stabilizes larger structures. At lower temperature and higher partial pressure of oxygen, the zeolite is very humid, both adsorbed and free water molecules are present when temperature decreases. However, for experimentally relevant temperatures and pressures, only the Cu_2O and the Cu_2OH are thermodynamically feasible active site configurations. With the two most stable active site motives identified, the reaction mechanism over the two sites was investigated in **Paper II**.

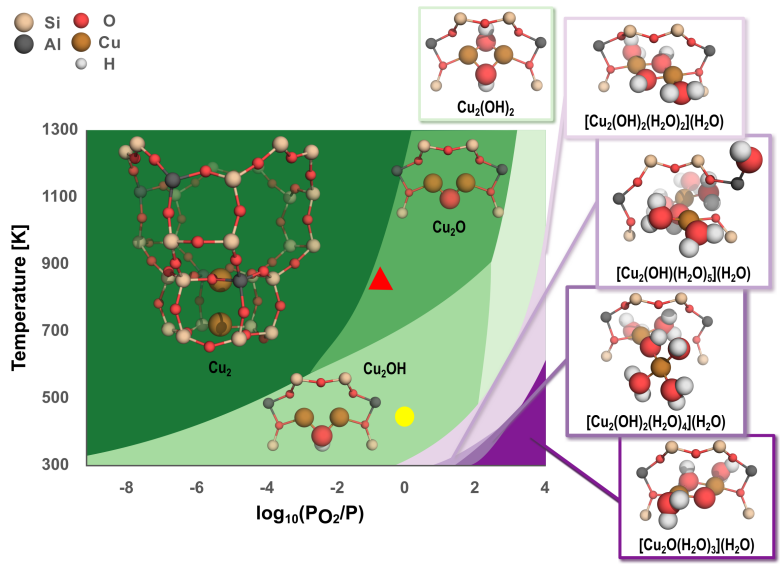

Figure 5.10: Phase diagram of oxidized Cu_2-clusters in SSZ-13. At higher temperature and lower partial pressure (top left corner), the Cu_2 situated inside the double 6MR is the most stable configuration. Decreasing temperature and increasing the partial pressure of O_2 means forming first to Cu_2O, and then Cu_2OH and $Cu_2(OH)_2$ clusters. At lower temperature and higher pressures, the cage becomes very humid. The red triangle (848 K, 20% O_2, 10^{-8}% H_2O) corresponds to activation conditions, and the yellow circle (448 K, 4% H_2O, 10^{-8}% O_2) corresponds to the conditions of extraction [132].

5.3.2 Partial methane oxidation over Cu_2O and Cu_2OH (Paper II)

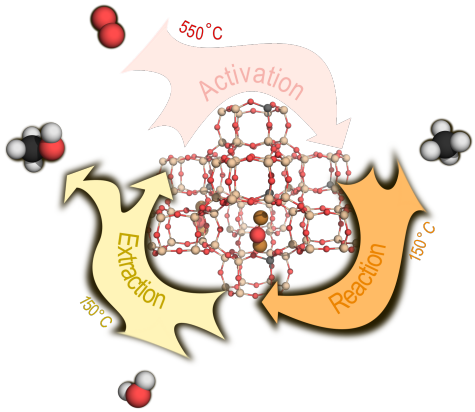

Figure 5.11: In **Paper II**, the mechanism for partial oxidation of methane is investigated over the most stable Cu dimer motifs in Cu-SSZ-13.

The main steps of the reaction are the same over both $Z_2[Cu_2O]$ (solid paths in fig. 5.12) and the $Z_2[Cu_2OH]$ (dashed paths in fig. 5.12): activation of the C-H bond in CH_4; rotation of reactants through the 8MR to form an adsorbed CH_3OH; and desorption of the CH_3OH molecule. This is true for the dry reaction paths (green paths in fig. 5.12) as well as when water is included into the mechanism (purple paths in fig. 5.12). As the H_2O molecule is added in the extraction phase of the reaction, it does not form part of the products and thus, mostly affects the energies of the intermediates and not the mechanism itself. The first TS in the reaction comes from the splitting of the C-H bond in CH_4 via the formation of a methyl radical. It has been debated whether this TS is actually the short-lived, highly reactive CH_3-radical, or rather a surface stabilized CH_3-group. Here, the radical TS was significantly more difficult to find, but once identified it has the lower energy. Formation of the methyl radical (TS1), is the highest barrier in the reaction over both sites. TS2 is only present in the $Z_2[Cu_2O]$ due to the orientation of the reactants in the 8MR. Over $Z_2[Cu_2O]$, the methyl radical first adsorbs to the Cu dimer before CH_3OH is formed, thus displaying TS2; while on the $Z_2[Cu_2OH]$ system the CH_3OH is formed straight from the radical. When considering the effect of water in the reaction landscape, the $Z_2[Cu_2O]$ and $Z_2[Cu_2OH]$ mechanisms have the opposite reaction. CH_3OH desorption in $Z_2[Cu_2O]$ is facilitated by water, but in $Z_2[Cu_2OH]$ it is hindered. Two lone Cu atoms are preferably separated and positioned in the 6MRs; however, as soon as the Cu atoms are connected, as with the hydrogen in *H, the cluster prefers to be in the 8MR. Thus, the positive effect of water on the dry system might be due to the stabilizing effect of the H_2O molecule on the * intermediate in the 8MR. Possibly, $Z_2[Cu_2OH]$ might react differently to a different solvent. The direct methane to methanol reaction follows the same basic steps over the Cu_2O site in SSZ-13 and in ZSM-5. The yellow line in fig. 5.12 shows the reaction path over Cu-ZSM-5 adapted from Arvidsson et al. [120]. The Cu-ZSM-5 is consistently lower in free energy, and especially the important

first barrier, TS1, is lower in the large pore zeolite. In addition, the desorption of the products is easier in Cu-ZSM-5, even more so than when water is added to Cu-SSZ-13. This despite the dry reaction conditions over Cu-ZSM-5.

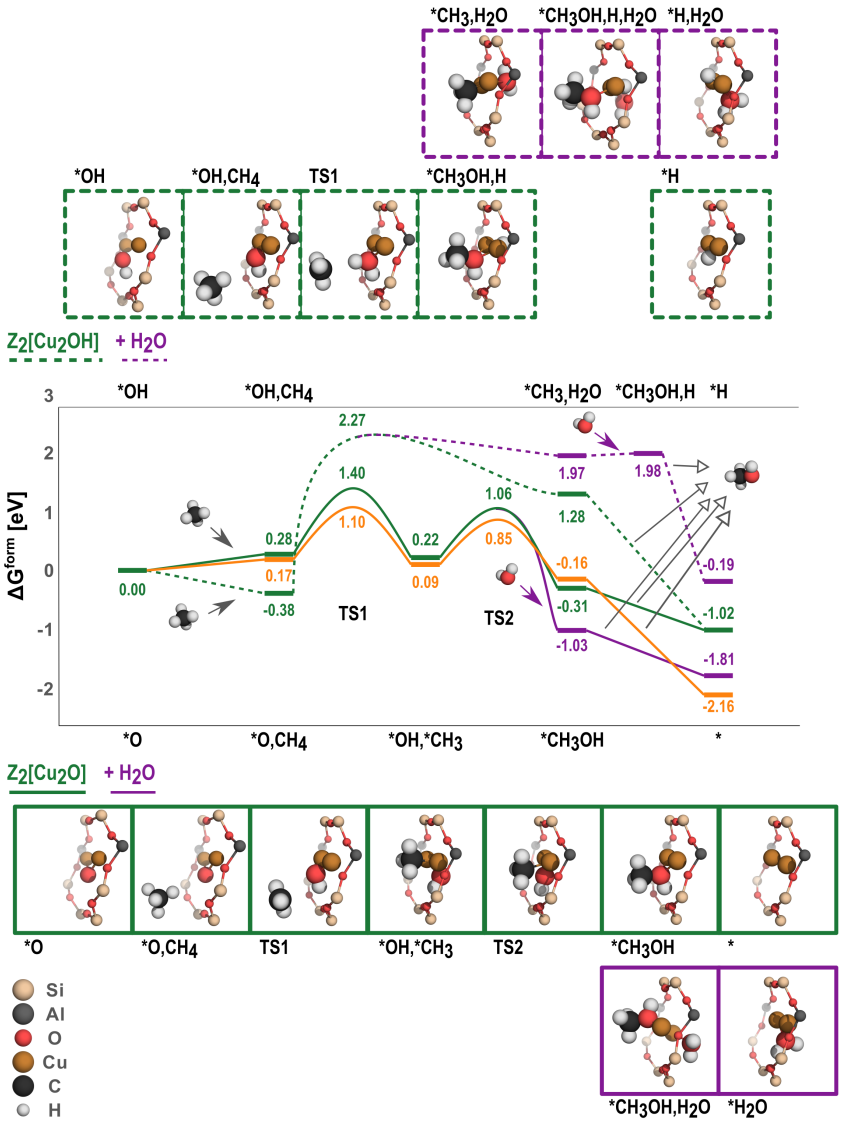

Figure 5.12: Reaction path over $Z_2[Cu_2O]$ in SSZ-13 (solid lines) and $Z_2[Cu_2OH]$ (dashed lines). Green shows the reaction during dry conditions and the purple path includes one water molecule in the reaction. The solid orange line is the reaction over $Z_2[Cu_2O]$ in ZSM-5 (adapted from [120]). Reaction conditions are set to T=448 K, 2% CH_4, 10% H_2O,10^{-9}% CH_3OH, with respect to atmospheric pressure.

The activity of the reaction mechanisms in fig. 5.12 is compared using a microkinetic model in fig. 5.13. The microkinetic model follows the result of the free energies in fig. 5.12, showing that neither of the dry sites in SSZ-13 are particularly good candidates for methane to methanol conversion. Clearly neither the $Z_2[Cu_2O]$ nor $Z_2[Cu_2OH]$ motifs, are likely responsible for any activity in the material. However, when water is added to the $Z_2[Cu_2O]$ site, the site experiences a large increase in activity, becoming a viable option as the active site motif. For the temperature range shown, the $Z_2[Cu_2O]$ MFI structure is the most active site. This contrasts with experimental results indicating a higher yield from the small pore zeolite system. Thus, one might draw the conclusion that the identified active site in the CHA is not the site responsible for the highest activity.

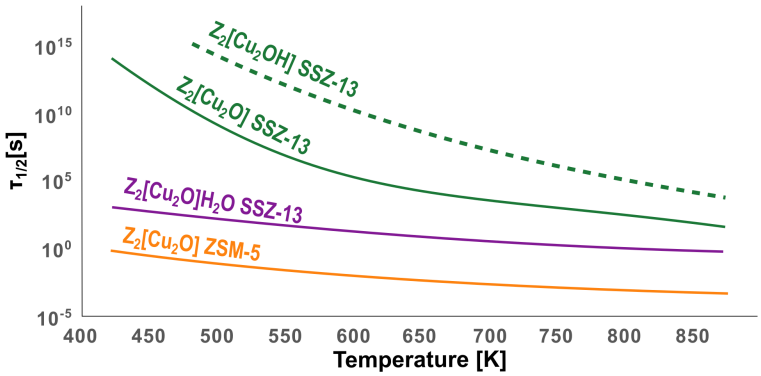

Figure 5.13: The active site half-time as a function of temperature. The $Z_2[Cu_2OH]$, $Z_2[Cu_2O]$, and $Z_2[Cu_2O]H_2O$ sites in SSZ-13 are here compared to that of the same reaction performed over the $Z_2[Cu_2O]$ site in the large pore zeolite ZSM-5 [120].

5.3.3 A complete reaction cycle over the dimer site in Cu-SSZ-13 (Paper III)

Concluding that the Cu_2OH site, along with the dry version of Cu_2O, does not contribute to the activity of the system leaves the $Cu_2O[H_2O]$ site as the only site energetically feasible during the reaction conditions which also shows activity towards the partial oxidation. To complete the reaction cycle, the formation of this active site must be considered. The low cost and abundance of O_2 make it the preferred oxidant in the reaction. From fig. 5.9, the Cu_2O_2 structure have a slightly positive formation energy for the considered conditions. However, since the structure of the active site is highly dependent on the exact chosen conditions, here the Cu_2O_2 structure will be considered as feasible. Thus, starting at the 2Cu structure, i.e., separated Cu atoms each residing in a 6MR, the oxygen molecule is used to activate the active site, followed by two methane to methanol reaction cycles, and lastly restructuring of the initial 2Cu structure. The identified reaction mechanism forms a fully catalytic cycle. The mechanism is performed with and without water (table 5.1), and as previous results indicate, when water is included, the activity of the site is increased.

Table 5.1: The elementary reactions used in the microkinetic model of the reaction over the sites in Cu-SSZ-13. The reaction over the first three sites corresponds to the dry reaction conditions, while the last three sites correspond to wet reaction conditions.

Site	Reaction			Type
$Z_2[2Cu]$	2Cu	$\rightleftharpoons$	Cu-pair	surface diffusion
	Cu-pair + O_2(g)	$\rightleftharpoons$	CuO_2Cu	adsorption
	CuO_2Cu	$\rightleftharpoons$	CuOOCu	surface reaction
$Z_2[CuOOCu]$	*2O + CH_4(g)	$\rightleftharpoons$	*2O,CH_4	adsorption
	*2O,CH_4	$\rightleftharpoons$	*O,CH_3OH	surface reaction
	*O,CH_3OH	$\rightleftharpoons$	*O + CH_3OH(g)	desorption
$Z_2[CuOCu]$	*O,CH_4(g)	$\rightleftharpoons$	*O,CH_4	adsorption
	*O,CH_4	$\rightleftharpoons$	*OH,*CH_3	surface reaction
	OH,CH_3	$\rightleftharpoons$	*CH_3OH	surface reaction
	*CH_3OH	$\rightleftharpoons$	* + CH_3OH(g)	desorption
$Z_2[2Cu]H_2O$	2Cu	$\rightleftharpoons$	Cu-pair	surface diffusion
	Cu-pair + O_2(g)	$\rightleftharpoons$	CuO_2Cu	adsorption
	CuO_2Cu	$\rightleftharpoons$	CuOOCu	surface reaction
$Z_2[CuOOCu]H_2O$	*2O + CH_4(g)	$\rightleftharpoons$	*2O,CH_4	adsorption
	*2O,CH_4	$\rightleftharpoons$	*O,CH_3OH	surface reaction
	*O,CH_3OH	$\rightleftharpoons$	*O + CH_3OH(g)	desorption
$Z_2[CuOCu]H_2O$	*O,CH_4(g)	$\rightleftharpoons$	*O,CH_4	adsorption
	*O,CH_4	$\rightleftharpoons$	*OH,*CH_3	surface reaction
	OH,CH_3	$\rightleftharpoons$	*CH_3OH	surface reaction
	*CH_3OH	$\rightleftharpoons$	* + CH_3OH(g)	desorption

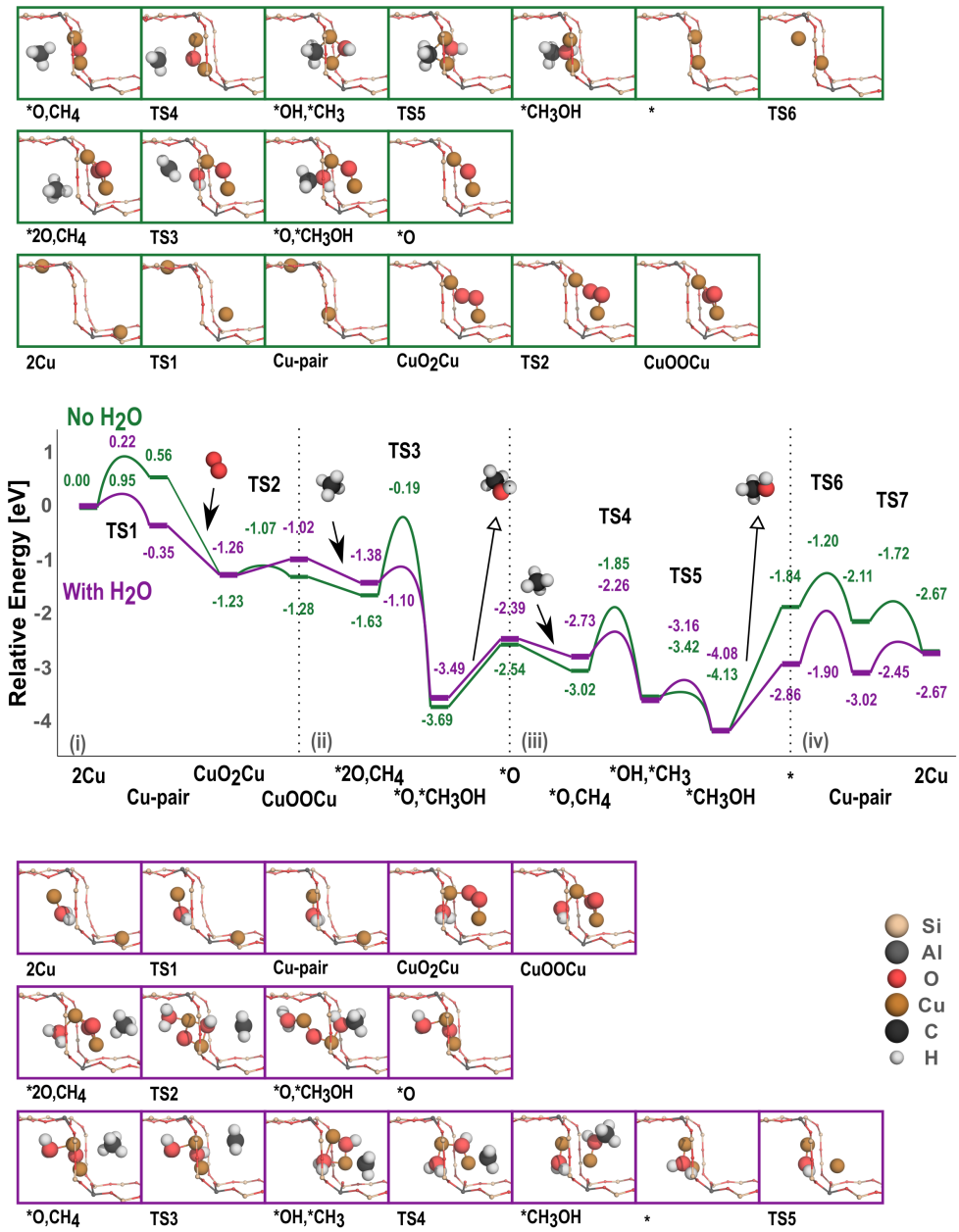

Figure 5.14: Reaction path over Z_2[2Cu] in SSZ-13. Green shows the reaction during dry conditions and the purple path includes one water molecule in the reaction. The solid lines represent the quasi-catalytic conditions, while the dashed lines show the energies during fully catalytic reaction conditions.

For simplicity, the complete cycle was divided into four parts, (i) the activation phase, which forms Cu dimers from two separate Cu ions (2Cu), (ii) the first reaction phase where methane interacts with CuOOCu and produce methanol, (iii) the second reaction phase where methane interacts with CuOCu and produce methanol, and finally (iv) the restructuring phase, where the formation of separate Cu ions occurs after desorbing the second methanol in the cycle. In fig. 5.14, the entirety of the reaction mechanism along with intermediate structures, for conditions with H_2O (green line) and without H_2O (purple line), is shown. The reaction path is mostly positively affected by the addition of water, and here it becomes clear that the activation phase (phase (i)) is benefited by the addition of water as the barriers for migrating the metal atoms along the framework and reshaping the active site structure, are lowered.

The effect of reaction conditions

The activity of the reaction mechanisms in fig. 5.12 is, again, compared using a microkinetic model based on the reactions in table 5.1. To further investigate the importance of water in the reaction, a model allowing both the dry and the wet mechanism to occur is used, and the calculated TOF is shown in fig. 5.15. Even a very low humidity (10^{-7} bar) gives an industrially viable TOF of 1 s^{-1} at the experimentally relevant temperature of 450 K. Based on the high activity identified on the active site, the reaction mechanism identified is likely hindered by CO and CO_2 formation, or formation of longer carbon chains such as DME. This is possible as the selectivity of the active site is not investigated, and all products are assumed to be methanol. However, the high activity towards methanol indicates that the Cu dimer is a potential active site for the reaction.

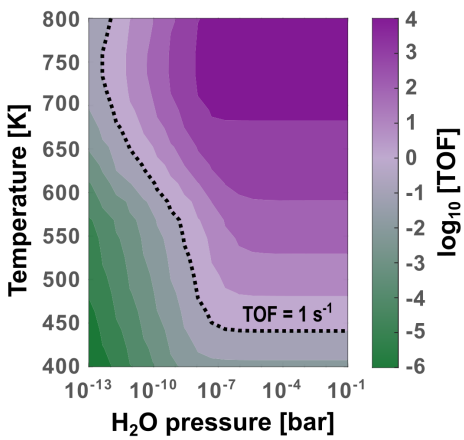

Figure 5.15: Logarithm of the TOF as a function of temperature and the partial pressure of water for combined wet and dry mechanisms with $p_{CH_4} = 2\%$, $p_{O_2} = 10\%$, $p_{CH_3OH} = 10^{-9}\%$ at atmospheric pressure after 10^6 s. The dotted contour highlights the conditions for which TOF = 1 s^{-1}.

Currently, the most common experimental procedure is a quasi-catalytic cycle, where the temperature is increased to facilitate activation of the oxidant. In fig. 5.16, the free energy of formation for the dry and wet reaction conditions is compared over the quasi-catalytic reaction conditions (823 K during activation, 423 K during reaction and extraction) and the fully catalytic conditions (490 K, 20% O_2, 4% CH_4 throughout the mechanism). The most pronounced effect of a quasi-catalytic approach is the destabilization of intermediate species. As all intermediate states have an exergonic formation, destabilization reduces the risk of poisoning the catalyst. During phases (ii) and (iii), a notable effect of the quasi-catalytic conditions is the removal of TS2, TS3, TS4, and TS5. Most notably, both barriers associated with activation of the CH_4 molecule, formation of the methyl radical, disappear when the conditions change. Over the CuOOCu site, this comes at a higher cost of introducing O_2 and CH_4 into the zeolite cage. However, the model used does not include diffusion of reactants inside the zeolite; thus, the cost of moving reactants to the active site is not taken into consideration, something which might affect the cost of introducing new reactants.

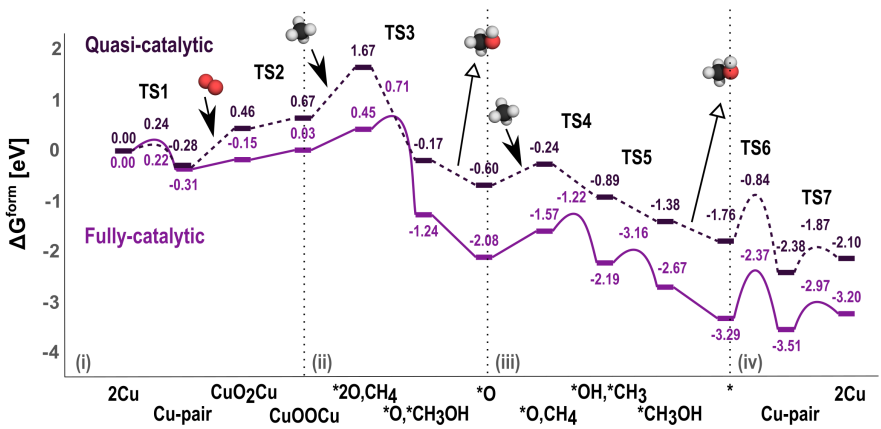

Figure 5.16: Comparison between the fully-catalytic reaction at 490K and the quasi-catalytic reaction where the temperature change along the reaction during wet conditions. Quasi-catalytic, dashed line: 823 K, O_2 20%, 10^{-9}% CH_4 during (i) and (vi); 423 K, CH_4 4%, 10^{-9}% O_2 during (ii) and (iii). Fully-catalytic, solid line: 490 K, O_2 20%, CH_4 2% during entirety of reaction.

Comparing experimental conditions shows the importance of the chosen reaction conditions. Consequently, reaction conditions can be adapted to stabilize desired active site structures, implying that the active site structure will change when conditions change, including along the reaction path. Common experimental procedures not applied in this study are purging with He and using a combination of gases to facilitate the different steps in the reaction [116]. A range in pressure for reactants, as well as the addition of different purging agents and solvents, would need to be investigated in order to optimize the reaction conditions for this active site structure.

5.3.4 Transition metal dimer sites in Chabazite (Paper IV)

Concluding that the Cu dimer structure is an active structure in the Chabazite framework opens up the question if other elements could have the same intermediate structures and also be active. Reasonably, these other structures might also be transition metals. The elements chosen for testing are Au, Ag since they are d^{10} elements just like Cu; Pd, Fe, Co since they have all shown the ability to do the partial oxidation reaction [117], [118], [133]; Ni, Zn since they are the elements used in the industrial steam reforming and syngas to methanol conversion. All reaction paths are based on the path identified for Cu, and the intermediate states are only locally optimized using the new elements. Thus, some of the elements do not seem to follow the same reaction paths, or exhibit the same intermediate structures as Cu. One such example is Ag. When performing the local optimization of Ag, the interatomic distances in the cluster exceed those of the Cu structures, causing the Ag structure to not fit inside the 8MR where the reaction is taking place for Cu. This leads to the conclusion that the identified reaction path for Cu does not work for Ag. The general reaction steps are likely similar, but the structure and placement of the active site inside the zeolite would have to be reoptimized specifically for the Ag dimer to present a more reliable energy profile for the reaction. Fe, Ni, Co, and Zn show a propensity to oxidize, forming very stable MeOOMe and MeOMe structure. Thus, the formation of methanol over these sites is unlikely. Based on the reaction landscape and stable intermediate structures, the elements most likely to follow a similar reaction path as Cu, are Au and Pd. In fig. 5.17 the energy landscapes of Cu, Au, and Pd, along with their alloys, are shown during wet conditions.

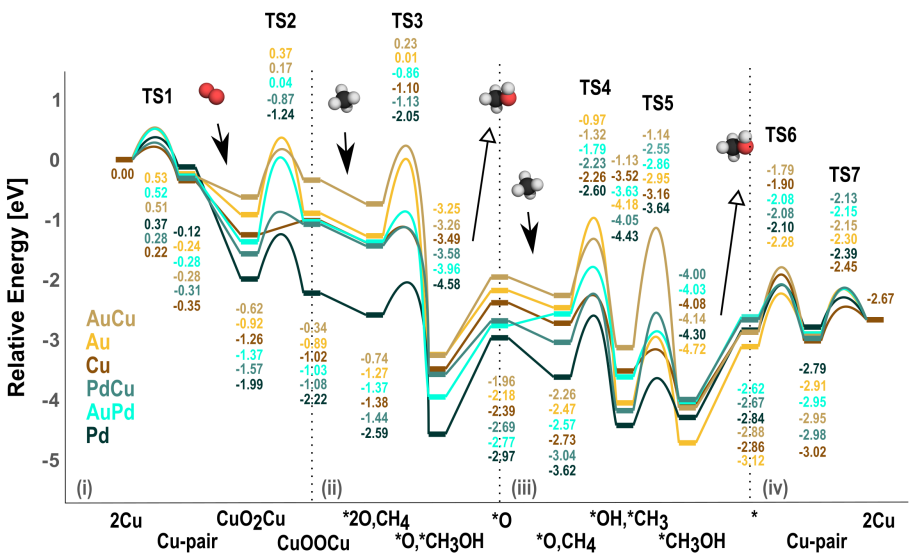

Figure 5.17: Reaction path over the Cu, Au, and Pd dimers and their alloys in SSZ-13 during wet reaction conditions.

The highest barriers in the reaction belong to the Au and AuCu systems. As all TS are higher for these systems than for, for instance Cu, these most likely does not have a competitive activity for the reaction. The Pd system has the most stable intermediate states, thus running the risk of poisoning the catalyst. The Cu, AuPd, and PdCu intermediate states all lie close in energy, displaying a similar energy profile. Based on the similarities in the energy landscape of the reaction, Cu, PdCu, and PdAu, should be comparable in activity for the reaction.

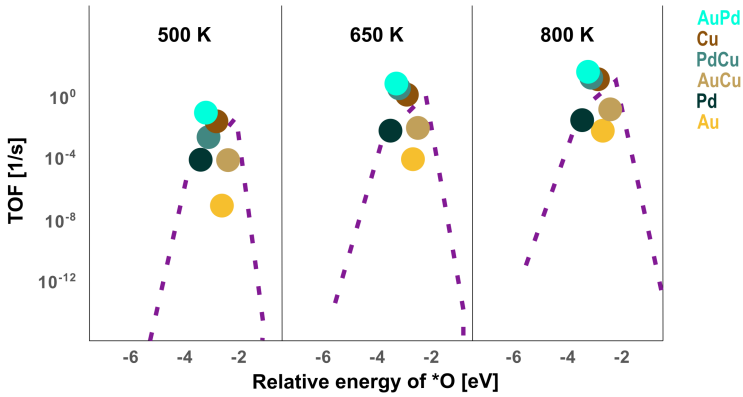

Figure 5.18: Comparison of kinetic predictions for the scaling relations and first-principles based models under wet conditions. Dashed lines show the scaling relations-based model results and markers show the first-principles based model results for each metal/metal alloy.

Using the descriptor of the adsorption energy of atomic oxygen, *O, scaling relations of the TOF of the systems at different temperatures are introduced. Using the scaling relations as input to the microkinetic model, Cu, AuPd, and PdCu, are close to the top of the volcano in fig. 5 .18. Only allowing for formation of methanol, the three most active candidates, Cu, AuPd, and PdCu, all display a TOF sufficient to render them industrially relevant for direct methane to methanol conversion.

Chapter 6

Concluding remarks

In this thesis, a few steps have been taken towards a deeper understanding of what system might constitute a functioning catalyst for the direct conversion of methane to methanol. However, several fundamental limitations have been set to the model. In terms of the structure of the catalyst, the full range of properties in the zeolite have not been explored as only one structure, CHA, have been considered; along with only Al substitution into the framework, one Si:Al ratio, one Al configuration, one Al:Cu ratio, and one active site configuration at the time. Using DFT to investigate all possible versions of the framework of only one zeolite structure would put a big strain on both human and computational time. To this purpose, a better option might be to use a genetic algorithm to investigate the phase space in a more efficient manner. With the choices made for the zeolite framework, **Paper I**, **Paper II**, and **Paper III** investigated the stability and activity of the two Cu atoms in SSZ-13 using ab initio thermodynamics and microkinetic modeling. The structure of the active site in the zeolite is found to be highly dependent on temperature and pressure. At low temperature conditions, a plethora of active site motifs are energetically feasible, and the system is likely to be very humid. This is in good correspondence with what has been known about zeolites since their discovery [134]. However, increasing the temperature makes the water leave the system, thereby reducing the number of energetically available active site structures. This highly dynamic nature of the active site is not fully included in further studies of the active site activity; as one configuration of the site is chosen, the constituent of the active site is not allowed to change other than to include the reactants and allow desorption of products. The inherent humidity of the system turns out to be an important factor for whether the partial oxidation reaction is thermodynamically feasible or not. The presence of water has a pronounced effect on the entirety of the reaction mechanism as it increases the mobility of the atoms in the active site, thus changing the barriers and desorption energies. When water is added to the reaction only one H_2O molecule is included in the cage and its position is optimized for each intermediate state; however, it functions simply as a spectator species, taking no active part in the reaction. As an adsorbate on the active site, it affects the stability of the reaction intermediates, but water is never directly involved in the formation of the products. This contrasts with experimental studies proposing water as the oxidant in the reaction [106]. Further, the added water is present during the entirety of the mechanism, i.e., there is no explicit extraction phase during the mechanism. As **Paper IV** indicates, the effect of water is not always for the benefit of the desired reaction. This is something not investigated further in this work, although it is a further indication that the optimum active site structure depends on the reaction conditions chosen, here including what solvent is used in the reaction. This nonuniform reaction to the presence of water also indicates the possibility of different

active sites interacting and enhancing different steps in the reaction mechanism. The limitation of a small (12 or 36 T-sites) unit cell only allows for one active site structure in each calculation, thus making the investigation of the interaction between active sites of different structures impossible. In **Paper I** and **Paper II**, the smallest 12 T-sites unit cell is used, but in **Paper III** and **Paper IV**, the 36 T-site unit cell is instead chosen. This is not considered when deciding on an active site structure, the same site structure is assumed to be energetically preferred regardless of active site concentration in the system. In **Paper IV**, the alloying of different metal alloys indicates that the atoms of the active site interact with the reactants individually rather than as a unit. This might be an effect of the limited size of the active cluster. There is only one path in the identified reactions mechanism in **Paper II**, **Paper III**, and **Paper IV**. Methanol is the only allowed product. No other products are formed over the active sites, thus neglecting the possible effect and function of the selectivity of the active site. To make a more encompassing study, side reactions and further oxidation of methane should be allowed to occur, enabling an investigation into the selectivity of the active site structures.

The work in the thesis is not done in conjunction with any experimental study; regardless, it provides detailed energy paths and structural information on active site configurations and provides an idea of what elements might be worth investigating in future experiments.

Chapter 7

Acknowledgement

The research work in this thesis has been carried out at the Division of Chemical Physics at the Department of Physics and the Competence Center for Catalysis (KCK) at Chalmers University of Technology, Sweden.

This research is financially supported by the Knut och Alice Wallenberg fundation. The Competence Center for Catalysis is financially supported by Chalmers University of Technology, the Swedish Energy Agency and the member companies: AB Volvo, ECAPS AB, Johnson Matthey AB, Preem AB, Scania CV AB, Umicore Denmark ApS and Volvo Car Corporation AB. The calculations have been performed at C3SE (Göteborg) and Tetralith at NSC (Linköping) through a SNIC grant.

I would like to thank my main supervisor, Anders Hellman, and co-supervisor, Henrik Grönbeck, for their support and guidance. A special thanks to my collaborators, Adam Arvidsson, for all help with the first kinetic model, and Astrid Boje, thank you for your insight, all your help, and your patience! I would also like to thank all my colleagues at Chemical Physics, as well as the members of KCK and the KAW-group.
Finally, I thank my family, who has supported me through this work!

References

[1] United States Environmental Protection Agency (EPA), *Understanding Global Warming Potentials*.

[2] U.S. Energy Information Administration (EIA), *Driving Down Methane Leaks From The Oil and Gas Industry - A regulatory roadmap and toolkit*, 2021.

[3] A. Hellman, K. Honkala, S. Dahl, C. Christensen, and J. Nørskov, Ammonia Synthesis: State of the Bellwether Reaction, *Comprehensive Inorganic Chemistry II (Second Edition): From Elements to Applications*, **7**, 459–474, 2013. DOI: 10.1016/B978-0-08-097774-4.00725-7.

[4] J. M. Thomas, R. Raja, and D. W. Lewis, Single-Site Heterogeneous Catalysts, *Angewandte Chemie International Edition*, **44**, no. 40, 6456–6482, 2005. DOI: 10.1002/anie.200462473.

[5] I. Chorkendorff and J. Niemantsverdriet, *Concepts of Modern Catalysis and Kinetics*. Wiley, 2006, ISBN: 9783527605644.

[6] P. Sabatier, Hydrogénations et déshydrogénations par catalyse, *Berichte der deutschen chemischen Gesellschaft*, **44**, no. 3, 1984–2001, 1911. DOI: 10.1002/cber.19110440303.

[7] L. McCusker, F. Liebau, and G. Engelhardt, Nomenclature of structural and compositional characteristics of ordered microporous and mesoporous materials with inorganic hosts: (IUPAC recommendations 2001), *Microporous and Mesoporous Materials*, **58**, no. 1, 3–13, 2003. DOI: 10.1016/S1387-1811(02)00545-0.

[8] F. Göltl and J. Hafner, Structure and properties of metal-exchanged zeolites studied using gradient-corrected and hybrid functionals. I. Structure and energetics, *The Journal of Chemical Physics*, **136**, no. 6, 064501, 2012. DOI: 10.1063/1.3676408.

[9] J. K. Nørskov, T. Bligaard, J. Rossmeisl, and C. H. Christensen, Towards the computational design of solid catalysts, *Nature Chemistry*, **1**, 37–46, 2009. DOI: 10.1038/nchem.121.

[10] A. A. Latimer, A. R. Kulkarni, H. Aljama, J. H. Montoya, J. S. Yoo, C. Tsai, F. Abild-Pedersen, F. Studt, and J. K. Nørskov, Understanding trends in C–H bond activation in heterogeneous catalysis, *Nature Materials*, **16**, 225–229, 2017. DOI: 10.1038/nmat4760.

[11] G. Pacchioni, Modeling doped and defective oxides in catalysis with density functional theory methods: Room for improvements, *The Journal of Chemical Physics*, **128**, 182505, 2008. DOI: 10.1063/1.2819245.

[12] M. Born and R. Oppenheimer, Zur Quantentheorie der Molekeln, *Annalen der Physik*, **389**, no. 20, 457–484, 1927. DOI: 10.1002/andp.19273892002.

[13] D. R. Hartree, The Wave Mechanics of an Atom with a Non-Coulomb Central Field. Part I. Theory and Methods, *Mathematical Proceedings of the Cambridge Philosophical Society*, **24**, no. 1, 89–110, 1928. DOI: 10.1017/S0305004100011919.

[14] V. Fock, Näherungsmethode zur Lösung des quantenmechanischen Mehrkörperproblems, *Zeitschrift für Physik*, **61**, no. 1, 126–148, 1930. DOI: 10.1007/BF01340294.

[15] D. R. Hartree and W. Hartree, Self-Consistent Field, with Exchange, for Beryllium, *Proceedings of the Royal Society of London Series A*, **150**, no. 869, 9–33, 1935. DOI: 10.1098/rspa.1935.0085.

[16] J. C. Slater, The Theory of Complex Spectra, *Phys. Rev.*, **34**, 1293–1322, 1929. DOI: 10.1103/PhysRev.34.1293.

[17] P. Hohenberg and W. Kohn, Inhomogeneous Electron Gas, *Phys. Rev.*, **136**, B864–B871, 1964. DOI: 10.1103/PhysRev.136.B864.

[18] J. Sakurai and J. Napolitano, *Modern Quantum Mechanics*. Addison-Wesley, 2011, ISBN: 9780321503367.

[19] W. Kohn and L. J. Sham, Self-Consistent Equations Including Exchange and Correlation Effects, *Phys. Rev.*, **140**, A1133–A1138, 1965. DOI: 10.1103/PhysRev.140.A1133.

[20] J. Kohanoff, *Electronic Structure Calculations for Solids and Molecules: Theory and Computational Methods*. Cambridge University Press, 2006. DOI: 10.1017/CBO9780511755613.

[21] G. L. Oliver and J. P. Perdew, Spin-density gradient expansion for the kinetic energy, *Phys. Rev. A*, **20**, 397–403, 1979. DOI: 10.1103/PhysRevA.20.397.

[22] O. Gunnarsson and B. I. Lundqvist, Exchange and correlation in atoms, molecules, and solids by the spin-density-functional formalism, *Phys. Rev. B*, **13**, 4274–4298, 1976. DOI: 10.1103/PhysRevB.13.4274.

[23] J. Sun, M. Marsman, G. I. Csonka, A. Ruzsinszky, P. Hao, Y.-S. Kim, G. Kresse, and J. P. Perdew, Self-consistent meta-generalized gradient approximation within the projector-augmented-wave method, *Phys. Rev. B*, **84**, 035117, 2011. DOI: 10.1103/PhysRevB.84.035117.

[24] J. P. Perdew, J. A. Chevary, S. H. Vosko, K. A. Jackson, M. R. Pederson, D. J. Singh, and C. Fiolhais, Atoms, molecules, solids, and surfaces: Applications of the generalized gradient approximation for exchange and correlation, *Phys. Rev. B*, **46**, 6671–6687, 1992. DOI: 10.1103/PhysRevB.46.6671.

[25] D. C. Langreth and M. J. Mehl, Beyond the local-density approximation in calculations of ground-state electronic properties, *Phys. Rev. B*, **28**, 1809–1834, 1983. DOI: 10.1103/PhysRevB.28.1809.

[26] J. P. Perdew, K. Burke, and M. Ernzerhof, Generalized gradient approximation made simple, *Phys. Rev. Lett.*, **77**, 3865–3868, 1996. DOI: 10.1103/PhysRevLett.77.3865.

[27] J. P. Perdew, A. Ruzsinszky, G. I. Csonka, O. A. Vydrov, G. E. Scuseria, L. A. Constantin, X. Zhou, and K. Burke, Restoring the density-gradient expansion for exchange in solids and surfaces, *Phys. Rev. Lett.*, **100**, 136406, 2008. DOI: 10.1103/PhysRevLett.100.136406.

[28] S. Grimme, Accurate description of van der Waals complexes by density functional theory including empirical corrections, *Journal of Computational Chemistry*, **25**, no. 12, 1463–1473, 2004. DOI: 10.1002/jcc.20078.

[29] S. Grimme, Semiempirical GGA-type density functional constructed with a long-range dispersion correction, *Journal of Computational Chemistry*, **27**, no. 15, 1787–1799, 2006. DOI: 10.1002/jcc.20495.

[30] S. Grimme, J. Antony, S. Ehrlich, and H. Krieg, A consistent and accurate ab initio parametrization of density functional dispersion correction (DFT-D) for the 94 elements H-Pu, *The Journal of Chemical Physics*, **132**, no. 15, 154104, 2010. DOI: 10.1063/1.3382344.

[31] A. D. Becke and E. R. Johnson, Exchange-hole dipole moment and the dispersion interaction, *The Journal of Chemical Physics*, **122**, no. 15, 154104, 2005. DOI: 10.1063/1.1884601.

[32] M. Dion, H. Rydberg, E. Schröder, D. C. Langreth, and B. I. Lundqvist, Van der waals density functional for general geometries, *Phys. Rev. Lett.*, **92**, 246401, 2004. DOI: 10.1103/PhysRevLett.92.246401.

[33] T. Thonhauser, V. R. Cooper, S. Li, A. Puzder, P. Hyldgaard, and D. C. Langreth, Van der waals density functional: Self-consistent potential and the nature of the van der waals bond, *Phys. Rev. B*, **76**, 125112, 2007. DOI: 10.1103/PhysRevB.76.125112.

[34] P. Hyldgaard, K. Berland, and E. Schröder, Interpretation of van der waals density functionals, *Phys. Rev. B*, **90**, 075148, 2014. DOI: 10.1103/PhysRevB.90.075148.

[35] A. D. Becke, Density-functional thermochemistry. III. The role of exact exchange, *The Journal of Chemical Physics*, **98**, no. 7, 5648–5652, 1993. DOI: 10.1063/1.464913.

[36] J. Heyd, G. E. Scuseria, and M. Ernzerhof, Hybrid functionals based on a screened Coulomb potential, *The Journal of Chemical Physics*, **118**, no. 18, 8207–8215, 2003. DOI: 10.1063/1.1564060.

[37] K. Terakura, T. Oguchi, A. R. Williams, and J. Kübler, Band theory of insulating transition-metal monoxides: Band-structure calculations, *Phys. Rev. B*, **30**, 4734–4747, 1984. DOI: 10.1103/PhysRevB.30.4734.

[38] S. L. Dudarev, G. A. Botton, S. Y. Savrasov, C. J. Humphreys, and A. P. Sutton, Electron-energy-loss spectra and the structural stability of nickel oxide: An LSDA+U study, *Phys. Rev. B*, **57**, 1505–1509, 1998. DOI: 10.1103/PhysRevB.57.1505.

[39] A. H. Larsen, M. Vanin, J. J. Mortensen, K. S. Thygesen, and K. W. Jacobsen, Localized atomic basis set in the projector augmented wave method, *Phys. Rev. B*, **80**, 195112, 2009. DOI: 10.1103/PhysRevB.80.195112.

[40] H. J. Monkhorst and J. D. Pack, Special points for brillouin-zone integrations, *Phys. Rev. B*, **13**, 5188–5192, 1976. DOI: 10.1103/PhysRevB.13.5188.

[41] P. Schwerdtfeger, The Pseudopotential Approximation in Electronic Structure Theory, *ChemPhysChem*, **12**, no. 17, 3143–3155, 2011. DOI: 10.1002/cphc.201100387.

[42] E. S. Sachs, J. Hinze, and N. H. Sabelli, Frozen core approximation, a pseudopotential method tested on six states of nah, *The Journal of Chemical Physics*, **62**, no. 9, 3393–3398, 1975. DOI: 10.1063/1.430993.

[43] G. Kresse and J. Hafner, Ab Initio molecular dynamics for liquid metals, *Phys. Rev. B*, **47**, no. 1, 558–561, 1993. DOI: 10.1103/PhysRevB.47.558.

[44] G. Kresse and J. Furthmüller, Efficiency of Ab-Initio Total Energy Calculations for Metals and Semiconductors Using a Plane-Wave Basis Set, *Computational Materials Science*, **6**, no. 1, 15–50, 1996. DOI: 10.1016/0927-0256(96)00008-0.

[45] G. Kresse and J. Furthmüller, Efficient Iterative Schemes for Ab Initio Total-Energy Calculations Using a Plane-Wave Basis Set, *Phys. Rev. B*, **54**, no. 16, 11169–11186, 1996. DOI: 10.1103/PhysRevB.54.11169.

[46] G. Kresse and J. Hafner, Norm-conserving and ultrasoft pseudopotentials for first-row and transition elements, *Journal of Physics Condensed Matter*, **6**, 8245–8257, 1994. DOI: 10.1088/0953-8984/6/40/015.

[47] G. Kresse and D. Joubert, From ultrasoft pseudopotentials to the projector augmented-wave method, *Phys. Rev. B*, **59**, 1758–1775, 1999. DOI: 10.1103/PhysRevB.59.1758.

[48] J. Klimeš, D. R Bowler, and A. Michaelides, Chemical accuracy for the Van der Waals density functional, *Journal of physics. Condensed matter*, **22**, 022201, 2010. DOI: 10.1088/0953-8984/22/2/022201.

[49] J. Klimeš, D. R. Bowler, and A. Michaelides, Van der Waals density functionals applied to solids, *Phys. Rev. B*, **83**, 195131, 2011. DOI: 10.1103/PhysRevB.83.195131.

[50] P. E. Blöchl, Projector augmented-wave method, *Phys. Rev. B*, **50**, 17953–17979, 1994. DOI: 10.1103/PhysRevB.50.17953.

[51] P. Debye, Näherungsformeln für die zylinderfunktionen für große werte des arguments und unbeschränkt veränderliche werte des index, *Mathematische Annalen*, **67**, no. 4, 535–558, 1909. DOI: 10.1007/BF01450097.

[52] M. R. Hestenes and E. L. Stiefel, Methods of Conjugate Gradients for Solving Linear Systems, *Journal of Research of the National Bureau of Standards*, **49**, 409–436, 1952. DOI: 10.6028/jres.049.044.

[53] S. T. W.H. Press B.P. Flannery and W. Vetterling, *Numerical Recipes*. Cambridge University Press, 1986.

[54] J. D. Head and M. C. Zerner, A Broyden-Fletcher-Goldfarb-Shanno optimization procedure for molecular geometries, *Chemical Physics Letters*, **122**, no. 3, 264–270, 1985. DOI: doi.org/10.1016/0009-2614(85)80574-1.

[55] C. G. Broyden, The Convergence of a Class of Double-rank Minimization Algorithms 1. General Considerations, *IMA Journal of Applied Mathematics*, **6**, no. 1, 76–90, 1970. DOI: 10.1093/imamat/6.1.76.

[56] R. Fletcher, A new approach to variable metric algorithms, *The Computer Journal*, **13**, no. 3, 317–322, 1970. DOI: 10.1093/comjnl/13.3.317.

[57] D. Goldfarb, A Family of Variable Metric Updates Derived by Variational Means, *Mathematics of Computation*, **24**, no. 109, 23–26, 1970. DOI: 10.1090/S0025-5718-1970-0258249-6.

[58] D. F. Shanno, Conditioning of quasi-Newton methods for function minimization, *Mathematics of Computation*, **24**, no. 111, 647–656, 1970. DOI: 10.1090/S0025-5718-1970-0274029-X.

[59] D. Liu and J. Nocedal, On the limited memory BFGS method for large scale optimization, English (US), *Mathematical Programming*, **45**, no. 3, 503–528, 1989. DOI: 10.1007/BF01589116.

[60] E. Bitzek, P. Koskinen, F. Gähler, M. Moseler, and P. Gumbsch, Structural Relaxation Made Simple, *Phys. Rev. Lett.*, **97**, 170201, 2006. DOI: 10.1103/PhysRevLett.97.170201.

[61] L. Verlet, Computer "Experiments" on Classical Fluids. I. Thermodynamical Properties of Lennard-Jones Molecules, *Phys. Rev.*, **159**, 98–103, 1967. DOI: 10.1103/PhysRev.159.98.

[62] W. C. Swope, H. C. Andersen, P. H. Berens, and K. R. Wilson, A computer simulation method for the calculation of equilibrium constants for the formation of physical clusters of molecules: Application to small water clusters, *The Journal of Chemical Physics*, **76**, no. 1, 637–649, 1982. DOI: 10.1063/1.442716.

[63] R. Barnett, U. Landman, A. Nitzan, and G. Rajagopal, Born-Oppenheimer dynamics using density-functional theory: Equilibrium and fragmentation of small sodium clusters, *Chemical Physics - CHEM PHYS*, **94**, 608–616, 1991. DOI: 10.1063/1.460327.

[64] R. Car and M. Parrinello, Unified Approach for Molecular Dynamics and Density-Functional Theory, *Phys. Rev. Lett.*, **55**, 2471–2474, 1985. DOI: 10.1103/PhysRevLett.55.2471.

[65] H. C. Andersen, Molecular dynamics simulations at constant pressure and/or temperature, *The Journal of Chemical Physics*, **72**, no. 4, 2384–2393, 1980. DOI: 10.1063/1.439486.

[66] H. J. C. Berendsen, J. P. M. Postma, W. F. van Gunsteren, A. DiNola, and J. R. Haak, Molecular dynamics with coupling to an external bath, *The Journal of Chemical Physics*, **81**, no. 8, 3684–3690, 1984. DOI: 10.1063/1.448118.

[67] S. C. Harvey, R. K.-Z. Tan, and T. E. Cheatham III, The flying ice cube: Velocity rescaling in molecular dynamics leads to violation of energy equipartition, *Journal of Computational Chemistry*, **19**, no. 7, 726–740, 1998.

[68] S. Nosé, A unified formulation of the constant temperature molecular dynamics methods, *The Journal of Chemical Physics*, **81**, no. 1, 511–519, 1984. DOI: 10.1063/1.447334.

[69] W. G. Hoover, Canonical dynamics: Equilibrium phase-space distributions, *Phys. Rev. A*, **31**, 1695–1697, 1985. DOI: 10.1103/PhysRevA.31.1695.

[70] D. J. Wales and J. P. K. Doye, Global Optimization by Basin-Hopping and the Lowest Energy Structures of Lennard-Jones Clusters Containing up to 110 Atoms, *The Journal of Physical Chemistry A*, **101**, no. 28, 5111–5116, 1997. DOI: 10.1021/jp970984n.

[71] D. Sheppard, R. Terrell, and G. Henkelman, Optimization methods for finding minimum energy paths, *The Journal of Chemical Physics*, **128**, no. 13, 134106, 2008. DOI: 10.1063/1.2841941.

[72] G. Henkelman and H. Jónsson, Improved tangent estimate in the nudged elastic band method for finding minimum energy paths and saddle points, *The Journal of Chemical Physics*, **113**, no. 22, 9978–9985, 2000. DOI: 10.1063/1.1323224.

[73] G. Henkelman, B. P. Uberuaga, and H. Jónsson, A climbing image nudged elastic band method for finding saddle points and minimum energy paths, *The Journal of Chemical Physics*, **113**, no. 22, 9901–9904, 2000. DOI: 10.1063/1.1329672.

[74] S. Smidstrup, A. Pedersen, K. Stokbro, and H. Jónsson, Improved initial guess for minimum energy path calculations, *The Journal of Chemical Physics*, **140**, no. 21, 214106, 2014. DOI: 10.1063/1.4878664.

[75] G. Henkelman and H. Jónsson, A dimer method for finding saddle points on high dimensional potential surfaces using only first derivatives, *The Journal of Chemical Physics*, **111**, no. 15, 7010–7022, 1999. DOI: 10.1063/1.480097.

[76] T. Hill, *An Introduction to Statistical Thermodynamics*, ser. Addison-Wesley series in chemistry. Dover Publications, 1986, ISBN: 9780486652429.

[77] J. Gibbs, A Method of Geometrical Representation of the Thermodynamic Properties of Substances by Means of Surfaces, *Transactions of the Connecticut Academy of Arts and Sciences*, **2**, 382–404, 1873.

[78] K. Reuter and M. Scheffler, Composition, structure, and stability of RuO_2(110) as a function of oxygen pressure, *Phys. Rev. B*, **65**, 1–11, 2001.

[79] A. H. Larsen, J. J. Mortensen, J. Blomqvist, I. E. Castelli, R. Christensen, M. Dułak, J. Friis, M. N. Groves, B. Hammer, C. Hargus, E. D. Hermes, P. C. Jennings, P. B. Jensen, J. Kermode, J. R. Kitchin, E. L. Kolsbjerg, J. Kubal, K. Kaasbjerg, S. Lysgaard, J. B. Maronsson, T. Maxson, T. Olsen, L. Pastewka, A. Peterson, C. Rostgaard, J. Schiøtz, O. Schütt, M. Strange, K. S. Thygesen, T. Vegge, L. Vilhelmsen, M. Walter, Z. Zeng, and K. W. Jacobsen, The atomic simulation environment—a Python library for working with atoms, *Journal of Physics: Condensed Matter*, **29**, no. 27, 273002, 2017.

[80] S. R. Bahn and K. W. Jacobsen, An object-oriented scripting interface to a legacy electronic structure code, English, **4**, no. 3, 56–66, 2002. DOI: 10.1109/5992.998641.

[81] A. Jansen, *An Introduction to Kinetic Monte Carlo Simulations of Surface Reactions*, ser. Lecture Notes in Physics. Springer Berlin Heidelberg, 2010, ISBN: 9783642294884.

[82] H. Eyring, The Activated Complex in Chemical Reactions, *The Journal of Chemical Physics*, **3**, no. 2, 107–115, 1935. DOI: 10.1063/1.1749604.

[83] U.S. Energy Information Administration (EIA), *International energy outlook 2019*, 2019.

[84] U. D. of Health, H. S. .-. A. for Toxic Substances, and D. Registry, *Toxicological Profile For Gasoline*, 1995.

[85] N. J. D. of Health, *Hazardous Substance Fact Sheet: Methane*, 2011.

[86] M. Saunois, A. R. Stavert, B. Poulter, P. Bousquet, J. G. Canadell, R. B. Jackson, P. A. Raymond, E. J. Dlugokencky, S. Houweling, P. K. Patra, P. Ciais, V. K. Arora, D. Bastviken, P. Bergamaschi, D. R. Blake, G. Brailsford, L. Bruhwiler, K. M. Carlson, M. Carrol, S. Castaldi, N. Chandra, C. Crevoisier, P. M. Crill, K. Covey, C. L. Curry, G. Etiope, C. Frankenberg, N. Gedney, M. I. Hegglin, L. Höglund-Isaksson, G. Hugelius, M. Ishizawa, A. Ito, G. Janssens-Maenhout, K. M. Jensen, F. Joos, T. Kleinen, P. B. Krummel, R. L. Langenfelds, G. G. Laruelle, L. Liu, T. Machida, S. Maksyutov, K. C. McDonald, J. McNorton, P. A. Miller, J. R. Melton, I. Morino, J. Müller, F. Murguia-Flores, V. Naik, Y. Niwa, S. Noce, S. O'Doherty, R. J. Parker, C. Peng, S. Peng, G. P. Peters, C. Prigent, R. Prinn, M. Ramonet, P. Regnier, W. J. Riley, J. A. Rosentreter, A. Segers, I. J. Simpson, H. Shi, S. J. Smith, L. P. Steele, B. F. Thornton, H. Tian, Y. Tohjima, F. N. Tubiello, A. Tsuruta, N. Viovy, A. Voulgarakis, T. S. Weber, M. van Weele, G. R. van der Werf, R. F. Weiss, D. Worthy, D. Wunch, Y. Yin, Y. Yoshida, W. Zhang,

Z. Zhang, Y. Zhao, B. Zheng, Q. Zhu, Q. Zhu, and Q. Zhuang, The global methane budget 2000–2017, *Earth System Science Data*, **12**, no. 3, 1561–1623, 2020. DOI: 10.5194/essd-12-1561-2020.

[87] *Methane*, Accessed October 31, 2019.

[88] I. E. A. (IEA), *Outlook for biogas and biomethane - Prospects for organic growth*, 2020.

[89] U. E. I. Administration, *Liquefied natural gas*, 2020.

[90] L. Haraldson, *Methanol as fuel*, 2015.

[91] W. H. Organization, *Health and Safety Guide No. 105 - Methanol*, 1997.

[92] B. Lacerda de Oliveira Campos, K. Herrera Delgado, S. Wild, F. Studt, S. Pitter, and J. Sauer, Surface reaction kinetics of the methanol synthesis and the water gas shift reaction on $Cu/ZnO/Al_2O_3$, *React. Chem. Eng.*, **6**, 868–887, 2021. DOI: 10.1039/D1RE00040C.

[93] P. Spath and D. Dayton, "Preliminary screening — technical and economic assessment of synthesis gas to fuels and chemicals with emphasis on the potential for biomass-derived syngas", 2003.

[94] G. Chinchen, K. Waugh, and D. Whan, The activity and state of the copper surface in methanol synthesis catalysts, *Applied Catalysis*, **25**, no. 1, 101–107, 1986. DOI: 10.1016/S0166-9834(00)81226-9.

[95] M. Behrens, F. Studt, I. Kasatkin, S. Kühl, M. Hävecker, F. Abild-Pedersen, S. Zander, F. Girgsdies, P. Kurr, B.-L. Kniep, M. Tovar, R. W. Fischer, J. K. Nørskov, and R. Schlögl, The Active Site of Methanol Synthesis over $Cu/ZnO/Al_2O_3$ Industrial Catalysts, *Science*, **336**, no. 6083, 893–897, 2012. DOI: 10.1126/science.1219831.

[96] P. Rasmussen, M. Kazuta, and I. Chorkendorff, Synthesis of methanol from a mixture of H_2 and CO_2 on Cu(100), *Surface Science*, **318**, no. 3, 267–280, 1994. DOI: 10.1016/0039-6028(94)90101-5.

[97] J. Yoshihara and C. T. Campbell, Methanol Synthesis and Reverse Water–Gas Shift Kinetics over Cu(110) Model Catalysts: Structural Sensitivity, *Journal of Catalysis*, **161**, no. 2, 776–782, 1996. DOI: 10.1006/jcat.1996.0240.

[98] N. A. Elango, R. Radhakrishnan, W. A. Froland, B. J. Wallar, C. A. Earhart, J. D. Lipscomb, and D. H. Ohlendorf, Crystal structure of the hydroxylase component of methane monooxygenase from Methylosinus trichosporium OB3b, *Protein Science*, **6**, no. 3, 556–568, 1997. DOI: 10.1002/pro.5560060305.

[99] S. Sirajuddin and A. C. Rosenzweig, Enzymatic Oxidation of Methane, *Biochemistry*, **54**, no. 14, 2283–2294, 2015. DOI: 10.1021/acs.biochem.5b00198.

[100] A. Rosenzweig, C. Frederick, and S. e. a. Lippard, Crystal structure of a bacterial non-haem iron hydroxylase that catalyses the biological oxidation of methane, *Nature*, no. 366, 537–543, 1993. DOI: doi.org/10.1038/366537a0.

[101] M. Ross and A. Rosenzweig, A tale of two methane monooxygenases, *Journal of Biological Inorganic Chemistry*, **22**, 307–319, 2017.

[102] P. H. Yu Mao, Identification of the active sites and mechanism for partial methane oxidation to methanol over copper-exchanged CHA zeolites, *SCIENCE CHINA Chemistry*, **63**, no. 6, 850–859, 2020. DOI: 10.1007/s11426-019-9695-9.

[103] C. Paolucci, A. A. Parekh, I. Khurana, J. R. Di Iorio, H. Li, J. D. Albarracin Caballero, A. J. Shih, T. Anggara, W. N. Delgass, J. T. Miller, F. H. Ribeiro,

R. Gounder, and W. F. Schneider, Catalysis in a Cage: Condition-Dependent Speciation and Dynamics of Exchanged Cu Cations in SSZ-13 Zeolites, *Journal of the American Chemical Society*, **138**, no. 18, 6028–6048, 2016. DOI: 10.1021/jacs.6b02651.

[104] U. Engedahl, H. Grönbeck, and A. Hellman, First-Principles Study of Oxidation State and Coordination of Cu-Dimers in Cu-SSZ-13 during Methane-to-Methanol Reaction Conditions, *The Journal of Physical Chemistry C*, **123**, no. 43, 26145–26150, 2019. DOI: 10.1021/acs.jpcc.9b07954.

[105] C. J. Heard, L. Grajciar, and P. Nachtigall, The effect of water on the validity of Löwenstein's rule, *Chem. Sci.*, **10**, 5705–5711, 2019. DOI: 10.1039/C9SC00725C.

[106] A. Koishybay and D. F. Shantz, Water Is the Oxygen Source for Methanol Produced in Partial Oxidation of Methane in a Flow Reactor over Cu-SSZ-13, *Journal of the American Chemical Society*, **142**, no. 28, 11962–11966, 2020. DOI: 10.1021/jacs.0c03283.

[107] V. L. Sushkevich, D. Palagin, M. Ranocchiari, and J. A. van Bokhoven, Selective anaerobic oxidation of methane enables direct synthesis of methanol, *American Association for the Advancement of Science*, **356**, no. 6337, 523–527, 2017. DOI: 10.1126/science.aam9035.

[108] C. Hammond, M. M. Forde, M. H. AbRahim, A. Thetford, Q. He, R. L. Jenkins, N. Dimitratos, J. A. Lopez-Sanchez, N. F. Dummer, D. M. Murphy, A. F. Carley, S. H. Taylor, D. J. Willock, E. E. Stangland, J. Kang, H. Hagen, C. J. Kiely, and G. J. Hutchings, Direct Catalytic Conversion of Methane to Methanol in an Aqueous Medium by using Copper-Promoted Fe-ZSM-5, *Angewandte Chemie International Edition*, **51**, no. 21, 5129–5133, 2012. DOI: 10.1002/anie.201108706.

[109] U. Engedahl, A. A. Arvidsson, H. Grönbeck, and A. Hellman, Reaction Mechanism for Methane-to-Methanol in Cu-SSZ-13: First-Principles Study of the $Z_2[Cu_2O]$ and $Z_2[Cu_2OH]$ Motifs, *Catalysts*, **11**, no. 1, 2021. DOI: 10.3390/catal11010017.

[110] U. Engedahl, A. Boje, H. Ström, H. Grönbeck, and A. Hellman, Complete Reaction Cycle for Methane-to-Methanol Conversion over Cu-SSZ-13: First-Principles Calculations and Microkinetic Modeling, *The Journal of Physical Chemistry C*, **125**, no. 27, 14681–14688, 2021. DOI: 10.1021/acs.jpcc.1c04062.

[111] X. Wang, N. Martin, J. Nilsson, S. Carlson, J. Gustafson, M. Skoglundh, and P.-A. Carlsson, Copper-Modified Zeolites and Silica for Conversion of Methane to Methanol, *Catalysts*, no. 8, 545, 2018. DOI: 10.3390/catal8110545.

[112] M. J. Wulfers, S. Teketel, B. Ipek, and R. F. Lobo, Conversion of methane to methanol on copper-containing small-pore zeolites and zeotypes, *Chem. Commun.*, **51**, 4447–4450, 2015. DOI: 10.1039/C4CC09645B.

[113] R. J. Lewis, A. Bara-Estaun, N. Agarwal, S. J. Freakley, D. J. Morgan, and G. J. Hutchings, The Direct Synthesis of H_2O_2 and Selective Oxidation of Methane to Methanol Using HZSM-5 Supported AuPd Catalysts, *Catalysis Letters volume*, **127**, no. 5, 1394–1395, 2005. DOI: 10.1021/ja047158u.

[114] P. Tomkins, M. Ranocchiari, and J. A. van Bokhoven, Direct Conversion of Methane to Methanol under Mild Conditions over Cu-Zeolites and beyond, *Accounts of Chemical Research*, **50**, no. 2, 418–425, 2017. DOI: 10.1021/acs.accounts.6b00534.

[115] K. T. Dinh, M. M. Sullivan, K. Narsimhan, P. Serna, R. J. Meyer, M. Dincă, and Y. Román-Leshkov, Continuous Partial Oxidation of Methane to Methanol Catalyzed by Diffusion-Paired Copper Dimers in Copper-Exchanged Zeolites, *Journal of the American Chemical Society*, **141**, no. 29, 11641–11650, 2019. DOI: 10.1021/jacs.9b04906.

[116] K. Narsimhan, K. Iyoki, K. Dinh, and Y. Román-Leshkov, Catalytic Oxidation of Methane into Methanol over Copper-Exchanged Zeolites with Oxygen at Low Temperature, *ACS Central Science*, **2**, no. 6, 424–429, 2016. DOI: 10.1021/acscentsci.6b00139.

[117] G. I. Panov, V. I. Sobolev, K. A. Dubkov, V. N. Parmon, N. S. Ovanesyan, A. E. Shilov, and A. A. Shteinman, Iron complexes in zeolites as a new model of methane monooxygenase, *Reaction Kinetics and Catalysis Letters*, **61**, 251–258, 1997. DOI: 10.1007/BF02478380.

[118] N. V. Beznis, B. M. Weckhuysen, and J. H. Bitter, Partial Oxidation of Methane Over Co-ZSM-5: Tuning the Oxygenate Selectivity by Altering the Preparation Route, *Catalysis Letters*, **136**, 52–56, 2010. DOI: 10.1007/s10562-009-0206-6.

[119] Z.-J. Zhao, A. Kulkarni, L. Vilella, J. K. Nørskov, and F. Studt, Theoretical Insights into the Selective Oxidation of Methane to Methanol in Copper-Exchanged Mordenite, *ACS Catalysis*, 3760–3766, 2016. DOI: 10.1021/acscatal.6b00440.

[120] A. A. Arvidsson, V. P. Zhdanov, P.-A. Carlsson, H. Grönbeck, and A. Hellman, Metal dimer sites in ZSM-5 zeolite for methane-to-methanol conversion from first-principles kinetic modelling: Is the [Cu–O–Cu]2+ motif relevant for Ni, Co, Fe, Ag, and Au?, *Catal. Sci. Technol.*, **7**, 1470–1477, 2017. DOI: 10.1039/C6CY02521H.

[121] B. Ipek, M. J. Wulfers, H. Kim, F. Göltl, I. Hermans, J. P. Smith, K. S. Booksh, C. M. Brown, and R. F. Lobo, Formation of $[Cu_2O_2]2+$ and $[Cu_2O]2+$ toward C–H Bond Activation in Cu-SSZ-13 and Cu-SSZ-39, *ACS Catalysis*, **7**, no. 7, 4291–4303, 2017. DOI: 10.1021/acscatal.6b03005.

[122] J. S. Woertink, P. J. Smeets, M. H. Groothaert, M. A. Vance, B. F. Sels, R. A. Schoonheydt, and E. I. Solomon, A $[Cu_2O]2+$ core in Cu-ZSM-5, the active site in the oxidation of methane to methanol, *Proceedings of the National Academy of Sciences*, **106**, no. 45, 18908–18913, 2009. DOI: 10.1073/pnas.0910461106.

[123] S. Grundner, M. A. Markovits, G. Li, M. Tromp, E. A. Pidko, E. J. Hensen, A. Jentys, M. Sanchez-Sanchez, and J. A. Lercher, Single-site trinuclear copper oxygen clusters in mordenite for selective conversion of methane to methanol, *Nature Communications*, **6**, no. 7546, 2015. DOI: 10.1038/ncomms8546.

[124] Y. Shiota and K. Yoshizawa, Methane-to-Methanol Conversion by First-Row Transition-Metal Oxide Ions: ScO+, TiO+, VO+, CrO+, MnO+, FeO+, CoO+, NiO+, and CuO+, *Journal of the American Chemical Society*, **122**, no. 49, 12317–12326, 2000. DOI: 10.1021/ja0017965.

[125] W. Löwenstein, The distribution of aluminum in the tetrahedra of silicates and aluminates, *American Mineralogist*, **39**, 92, 1954.

[126] H. Rydberg, B. I. Lundqvist, D. C. Langreth, and M. Dion, Tractable nonlocal correlation density functionals for flat surfaces and slabs, *Phys. Rev. B*, **62**, 6997–7006, 2000. DOI: 10.1103/PhysRevB.62.6997.

[127] H. Rydberg, M. Dion, N. Jacobson, E. Schröder, P. Hyldgaard, S. I. Simak, D. C. Langreth, and B. I. Lundqvist, Van der waals density functional for layered structures, *Phys. Rev. Lett.*, **91**, 126402, 2003. DOI: 10.1103/PhysRevLett.91.126402.

[128] K. Berland and P. Hyldgaard, Exchange functional that tests the robustness of the plasmon description of the van der waals density functional, *Phys. Rev. B*, **89**, 035412, 2014. DOI: 10.1103/PhysRevB.89.035412.

[129] J. Wellendorff, K. T. Lundgaard, A. Møgelhøj, V. Petzold, D. D. Landis, J. K. Nørskov, T. Bligaard, and K. W. Jacobsen, Density functionals for surface science: Exchange-correlation model development with bayesian error estimation, *Phys. Rev. B*, **85**, 235149, 2012. DOI: 10.1103/PhysRevB.85.235149.

[130] J. J. Mortensen, K. Kaasbjerg, S. L. Frederiksen, J. K. Nørskov, J. P. Sethna, and K. W. Jacobsen, Bayesian error estimation in density-functional theory, *Phys. Rev. Lett.*, **95**, 216401, 2005. DOI: 10.1103/PhysRevLett.95.216401.

[131] L. Y. Isseroff and E. A. Carter, Importance of reference Hamiltonians containing exact exchange for accurate one-shot *gw* calculations of Cu_2O, *Phys. Rev. B*, **85**, 235142, 2012. DOI: 10.1103/PhysRevB.85.235142.

[132] X. Wang, "Catalytic methane oxidation for emission control and fuel liquefaction", PhD thesis, Chalmers University of Technology, 2017.

[133] K. Dubkov, V. Sobolev, E. Talsi, M. Rodkin, N. Watkins, A. Shteinman, and G. Panov, Kinetic isotope effects and mechanism of biomimetic oxidation of methane and benzene on FeZSM-5 zeolite, *Journal of Molecular Catalysis A: Chemical*, **149**, 3066–3075, 2019. DOI: 10.1007/s10562-019-02876-7.

[134] A. F. Cronstedt, Om en obekant bärg art, som kallas zeolites, *Kongl. Svenska Vetenskaps Academiens Handlingar Stockholm*, **17**, 1756.